Technical Report No. 1

08160-1-T

HOLOGRAM INTERFEROMETRY IN CYLINDRICAL SHELL VIBRATION ANALYSIS

August 1967 to August 1968

ORL Subcontract R66-2476
Under Contract NOw-65-0123-d

Prepared by

Lyman W. Orr
Norman E. Barnett

Cooley Electronics Laboratory
Department of Electrical Engineering
The University of Michigan
Ann Arbor, Michigan

for

Ordnance Research Laboratory
The Pennsylvania State University
State College, Pennsylvania

December 1968

ABSTRACT

This report relates how hologram interferometry has been applied to the study of flexural vibrations of an end-supported uniform cylindrical shell. The interferograms have revealed detailed distributions of resonant vibrations on the shell and how they varied with frequency. These results have been correlated with total radiated sound-power measurements accomplished in the same small frequency increments found necessary during the interferometric studies.

The effects of adding a central stiffening rib to the shell have also been investigated using sound-power measurements correlated with interferometry. In one instance, the stiffening rib resulted in a more highly developed resonant mode, and this was accompanied by a twenty-fold increase in the radiated power.

In this report the section on interpretation of interferograms extends the theory relating to time-average holograms of sinusoidal steady-state vibrations. The concepts of an optical-sensitivity vector are developed and applied to the examination of highly curved surfaces. Methods for resolving ambiguities in time-average interferograms are presented as well as explanations of some of the unusual aspects of fringe patterns observed on the cylindrical shell. Various details relating to laboratory procedures for hologram interferometry are given in the appendixes.

TABLE OF CONTENTS

TABLE OF CONTENTS (Cont.)

LIST OF FIGURES

LIST OF FIGURES (Cont.)

LIST OF FIGURES (Cont.)

1. INTRODUCTION

Hologram interferometry of vibrating objects was first performed at The University of Michigan by Powell and Stetson in 1965 (Ref. 1). Shortly thereafter, their methods were adopted by this laboratory in conjunction with acoustical research for the study of vibrating structures, and a holographic laboratory facility was established. Since that time, the continued application of holographic methods has led to the development of refined techniques in both real-time and time-average interferometry, to the extension of these techniques to vibrating objects submerged in water, and to the development of analytical understanding in the interpretation of the interferograms.

To establish a background for the studies reported here, various investigations were undertaken to learn how to investigate mechanical vibrations effectively utilizing the new techniques of hologram interferometry. A large part of this underlying research was sponsored by the Ordnance Research Laboratory at The Pennsylvania State University, but concurrent studies under different sponsorship have also contributed significantly.

One early, extensive study made in 1966 of the vibrational modes of a clamped circular plate disclosed both the expected classical modes as well as several unpredicted modes of vibration. It also clearly

revealed consequences of material anisotropy and demonstrated how perturbations to a vibrating system could be studied. These results and others of similar nature were described to personnel of the Ordnance Research Laboratory in a technical briefing on January 19, 1967 and, in abridged form, to the Engineering Acoustics Seminar (Ref. 2) held the same day.

A cantilever beam was used for another set of interferometric investigations. One of the more dramatic consequences was a very clear display of anticlastic bending in this beam under dynamic vibrational conditions; probably the first time this classical behavior had actually been observed with photographic clarity.

Another direction of exploration was to find out if the methods of hologram interferometry could be applied to vibrating objects submerged in water. A previous experiment (Ref. 3) had demonstrated that ordinary holography of submerged objects was possible. The first good quality interferograms of a circular plate vibrating in water were obtained in early January 1967. Both real-time and time-average interferometry were accomplished through a total water path of approximately four feet and the quality of the holograms was fully as good as those for air. Thus the methods of hologram interferometry are available for investigating submerged vibrating structures as the needs arise. A reconstruction of one of the time-average, in-water interferograms was shown by one of us (Barnett) at the technical meeting on January 19, 1967 mentioned above.

A study of the vibrations of a piezoelectric ceramic disk in 1967 by time-average interferometry showed interference fringes which changed position with viewing direction. These fringes also displayed asymmetries which proved to be caused by the optical arrangement rather than by the vibration of the ceramic disk itself. These observations stimulated an analysis which explained the results and which gave rise to the concept of isophase surfaces. This concept has been valuable in approaching certain problems in hologram interferometry, both in arranging the optics and in interpreting the results. A letter to the editor of Applied Optics (Ref. 4) was written on this subject and permission for its publication was granted by ORL. The concept of a sensitivity vector developed from the isophase-surface concept and this new development is discussed in detail in Section 3. 2 of this report.

A technical paper (Ref. 5) which summarized many of our background results with respect to applied hologram interferometry was given before a national meeting of the Optical Society of America in November 1967, with permission from ORL. Most recently, an invited paper (Ref. 6) was presented at the Underwater Sound Laboratory, and this paper drew extensively upon the research reported here in detail.

Also, Dr. Wang of ORL was given a one-week laboratory course in hologram interferometry in our laboratory in the fall of 1967.

The various activities just described formed the technical background for the present research. They enabled us to develop an

understanding of hologram interferometry and how it may be applied to the investigation of vibrational problems. They were the vehicle for developing an effective laboratory procedure and the associated analytical techniques for interpretation. With this background, the present research program could be undertaken where the emphasis has shifted from problems in hologram interferometry to the problem of practical vibration analysis related to engineering noise control.

The bulk of this report deals with the experimental and analytical investigation of flexural vibrations in a long, end-supported cylindrical shell. Both real-time and time-average interferometry were used to study the distribution patterns of various vibrational modes, and these were correlated with radiated sound-power measurements made in the reverberation chamber. The effects of adding a central stiffening rib were also studied. In addition to the value of the experimental results, this work constitutes advances in both the technique and the interpretation of hologram interferometry for vibration analysis.

2. EXPERIMENTAL STUDIES

The principal experimental studies of this program have been of two types. First were the studies using hologram interferometry to reveal the vibrational displacements of cylindrical shells. These were the pathfinding studies in terms of learning how to exploit hologram interferometry for this particular application. Second were the measurements of total radiated sound power for the same shell modes which had been revealed holographically. These measurements explored the acoustical efficiency associated with the several modes of vibration.

Both types of studies are interesting and valuable in their own right. The ultimate acoustical engineering goal, however, is to be able to follow the flow of vibrational energy through shell structures. Such information would permit rational design-engineering with respect to vibration. The holographic investigation and the sound-power measurements constitute important steps toward that goal.

2.1 Holographic Studies

Much of the research effort was absorbed by the hologram interferometry studies. The methods of real-time interferometry (Appendix A) and time-average interferometry were utilized as needed. The more important results are presented by means of photographs, all of which

are reconstructions from the time-average interferograms. (All figures appear at the end of the text.)

The Ordnance Research Laboratory supplied a set of three cylindrical shells, dimensionally scaled, which they had used in previous research programs. We selected the middle-sized shell as most convenient for our initial experiments and, to date, it has been used exclusively. Figure 1 presents the important dimensions of this uniform steel shell.

Figure 2 illustrates how the shell was mounted for both the holographic studies and the sound-power measurements. The two ends were treated identically. The acoustical drivers became a permanent part of the mounting structure and supported the shell even when local magnetic excitation was used to drive the shell. Acoustical excitation was employed for most of the results reported. The two acoustical drivers were operated in phase so that they both generated positive pressures within the shell at the same instant of time.

A block diagram of the driving instrumentation is given in Fig. 3 while Appendix C. 1 identifies the particular instruments.

The method used to excite vibration in the shell structure merits further discussion. Acoustic excitation was selected for the present studies because it appeared capable of providing a more uniform radial force-field than any other method readily devised. Radial uniformity was desired so that the circumferential location of nodal lines would

represent natural shell behavior rather than arbitrarily chosen forced behavior. It was realized that, in general, the axial distribution of the exciting force would not be uniform. The possibility for varying the relative phase between the two drivers, either stepwise or continuously, offered a method for shifting the axial force distribution which might become important in future studies.

The method of fixed-phase acoustic-excitation was successful for present purposes in the sense that good holograms of the vibrational modes were obtained. However, techniques for applying the exciting forces to experimental shell structures require more study to satisfy the needs of future research in this same general problem area.

Figure 4 is a plan view of the holographic apparatus including the experimental shell. The apparatus was arranged so that the sensitivity vector (Section 3. 2) was normal to the shell on-axis and midway along its length. Thus, along the length of the shell and on-axis, variation in the magnitude and the direction of the sensitivity vector was minimized and the residual variation was symmetrical about the midpoint. The corresponding variation of the sensitivity vector above and below the axis was negligible also because the subtended angle (from, e.g., the viewing point) was small. Nevertheless, because the shell was strongly curved and because the shell's displacements were not constrained to lie in a radial direction, the detailed interpretation of off-axis interference fringes remains somewhat involved. (See Section 3. 4.)

The shell was located so that proper geometrical perspective could be obtained when photographing it from behind the hologram plate holder, which is the camera location when reconstructing time-average interferograms (Fig. 4). Among other considerations, this required that the film plane in the camera be positioned parallel to the shell's axis. Also, to avoid the need for very small lens apertures, the lens board was positioned parallel to the shell's axis with the lens shifted laterally to center the image on the film. Thus the camera lens only needed to be stopped down enough to obtain a depth-of-field equal to the shell's radius. In general, a correct camera setup is not particularly difficult to achieve with a versatile view camera and a selection of lenses. Only a 4 by 5 in. Crown Graphic with an f/ 4. 7, 5-3/ 8 in. lens was available for the present work, and its limited flexibility restricted the arrangement of the holographic setup.

Figure 5 is a photograph of the cylindrical shell taken in ordinary white light; camera location and adjustment were the same as used for the hologram reconstructions. Paper scales, marked in degrees, were wrapped around the shell to assist in interpreting the angular extent of interference patterns displayed in the reconstructions. The 90 degree marks are seen to be directly on-axis. Several other objects are visible in this picture and should be noted for future reference. Below the shell and to the left is a plastic number (a figure-8 turned to a 9 o'clock position in this case) used to number the holograms. A 3-inch long scale

appears under the shell. To the right is a section of aluminum tubing viewed diagonally. It extends from underneath the cylindrical shell to a position somewhat closer to the camera than any other important detail. The rendering of this aluminum tubing assisted us in judging the quality of the holograms, especially since its nearest edge darkened slightly due to almost exceeding the coherence length of the laser.

The photograph shows the acoustic drivers at each end of the shell. Wide-angle photographic perspective distortion has started to become apparent. Weak reflections of various objects are to be seen in the polished granite table surface. An 8 by 10 in. mirror lying flat on the granite table caused a reflection which shows a clear rendering of the central angular scale. This mirror view shows a portion of the under side of the cylindrical shell from about 112. 5 degrees around to 180 degrees. Note that in the interferogram reconstructions the sensitivity vector will be oriented differently for the mirror view than in the direct view. The interference patterns seen in the mirror can sometimes be used to assist the interpretation of the more complicated patterns. Behind the cylinder and to the right of center is the vertical rod of a ring stand used to support a magnetic driver behind the shell. This magnetic driver was used for some experiments and was positioned at several longitudinal locations. Other objects may be seen dimly in the background but are without consequence to the present research.

Figure 6 is a similar direct photograph of the shell illuminated in laser light by means of the subject beam (Fig. 4). This photograph provides a valid impression of the distribution of laser illumination which was effective when exposing the holograms.

2. 1. 1 Uniform Shell. Figure 7 is a composite photograph of a variety of mode patterns found during the initial survey studies of the uniform shell. Real-time interference holography was used to locate these regions of interest and then time-average interferograms were taken to provide a photographic record of what had been seen.

The two lowest frequency modes (170 Hz and 350 Hz) were undoubtedly beam-like vibrations involving the entire angle-plate-driver-shell system and were not investigated in detail. Starting at 1039 Hz, we first encountered flexural modes of vibration appropriate to the end-supported or end-stiffened cylindrical shell. Several of these modes could be excited to reasonably large amplitudes, and they were studied in more detail as described below. Figure 8, adapted from Arnold and Warburton (Ref. 7) shows the anticipated mode-frequency diagram for low-order modes.

The longitudinal mode number m denotes the number of half wavelengths of flexural vibration (i. e., the number of radial antinodes) along the length of the cylinder. The circumferential mode number n denotes the number of full wavelengths of flexural vibration (i. e., half the number of radial antinodes) around the circumference of the cylinder.

These shell modes had relatively large quality factors (Q's), and therefore excellent stability of the driving signal, both in amplitude and in frequency, became prerequisite to good time-average interferometry. Satisfactory stability became all the more difficult to obtain because the combined effects of low-film sensitivity, wide-angle light distribution, and relatively poor laser performance placed the exposure times in the range of 2-1/2 to 4 minutes. Most of the research was accomplished under this handicap, but near the end of the work, improved laser performance and a new higher speed photographic emulsion (Appendix B. 5) reduced our working exposures to less than 10 seconds. These shorter exposures greatly reduced the stability problems.

Figure 9 presents a composite of reconstructions from seven holograms made of shell vibration in the vicinity of mode $m = 1$, $n = 2$. Small increments in frequency of about one hertz were needed to display the progression of vibrational behavior. Note first that the mode is split (Section 3. 5). Split modes are fairly typical of real experimental systems as compared to their idealized theoretical counterparts. The same modal configuration will appear twice at slightly different frequencies; only the orientation of the nodal pattern will have shifted. In this case, the two frequencies are about 1035. 2 Hz and 1039. 2 Hz respectively. Moreover, each component of the split mode has a bandwidth which is probably less than one hertz so that the Q's are on the order of 1000.

As explained in Section 3. 2, the maximum sensitivity to radial motion would occur precisely on the centerline in these photographs due to the orientation of the sensitivity vector. At other positions on the shell, the dot product between the field of sensitivity vectors and the field of vibrational displacement vectors causes the dark interference fringes to represent differing amounts of actual vibrational displacement. Section 3 treats such considerations in detail. For the present discussion, it will suffice to consider the interferogram as a qualitative topographic map representing the vibrational displacements. One should not jump to the almost instantaneous intuitive interpretation of the actual vibrational displacement which similar interferograms of vibrating flat plates viewed normally will permit; a thorough appreciation of the considerations in Section 3 is needed to support both immediate intuitive reading, as well as fully detailed analysis, of interferograms of cylindrical shells. Indeed, these warnings apply to all vibrational interferograms except those of very simple, known vibrational behavior.

In Fig. 9 apparently neither a node or an antinode at resonance fell exactly across the centerline. It would have been necessary to rotate the cylinder about its axis in order to bring about that orientation. This could have been done, of course, but it was not convenient to do so, and the general characteristics of the split mode appear to be displayed clearly enough for present purposes. It remains questionable, nevertheless, whether any of the interferograms in this sequence were

taken with the excitation frequency tuned precisely to maximum-displacement response.

Figure 10 shows a similar group of interferograms for the mode m = 2, n = 2 which occurred in the vicinity of 1317 Hz. Obviously, the beginning and ending of this split mode lies beyond the encompassed range of frequencies because the end photographs each display two fringes of motion. The two frequencies for this split mode appear to be separated by only about two hertz. Between them, the vibrational response produces peculiar cusp-shaped interference fringes. The cusps appear because significant responses occur simultaneously for both components of the split mode and the phase differences between these responses produce an elliptical particle displacement on the shell. In the case of the split mode, m = 1, n = 2, described previously (Fig. 9), the two components were separated widely enough in frequency in consequence of the mode Q's to avoid generating cusp-shaped fringe patterns completely.

Several of the reconstructed interferograms are not rendered as brightly and clearly as might be desired. There is a tendency for the left-hand end of the shell to go dark. This darkening seems to be the result of lesser mechanical stability at the left-hand end of the shell than at the right-hand end. One contributing factor was thermal expansion as verified by the behavior of the real-time fringes. Even two or three watts of electrical power furnished to the acoustic drivers was enough

to expand the driver frames by several wavelengths of light after some appreciable time lag due to thermal inertia. Because the drivers were inside the angle plates, something had to move and usually it was the left-hand end of the apparatus. Our typical working procedure of first observing the real-time fringes and then taking a series of time-average holograms contributed to a gradual thermal buildup. The thermal instability became most noticeable part way through each work session. The long exposure times were especially unfavorable. In future work, the support structure probably should be modified to a more kinematical arrangement to improve the positional stability.

Figure 11 shows the next higher frequency mode, m = 3, n = 2, in the vicinity of 1943 Hz. Chronologically, this mode was the first one studied in fine detail which partially accounts for the large number of interferograms in the sequence. The left-hand end stability problem was relatively severe. The split-mode phenomenon was not displayed conspicuously, although some traces of it did appear. Cusp-shaped fringes can be observed near the middle of the picture.

Two other features are worth noting although they may not be fully repeatable with successive reassembly of the shell structure. The first observation is that appreciable response first appeared most strongly on the left-hand end of the shell but terminated at the right-hand end. One would expect such behavior to cause the radiated directionality pattern to undergo some gyrations as a function of frequency

compared to a theoretically spatially uniform pattern. Second, the central group of fringes (considering longitudinal position) is more compact than the end patterns. This difference looks larger than would be expected from the slightly shifting direction taken by the sensitivity vector. If a more complete analysis confirms this feature, it has implications both with respect to the mechanical end-conditions and with respect to the radiation pattern of a finite shell.

Figures 12 and 13 show vibrational behavior that has not been completely identified. At least two different catagories of phenomena are present. One is a natural consequence of the vibrational mode distribution for this particular cylindrical shell, a fact which was fully appreciated only long after the interferograms had been taken. The other is a consequence of unsolved experimental difficulties, mostly the same thermal expansion difficulty mentioned earlier.

The real vibrational phenomenon can be explained by referring back to Fig. 8. Frequency has been plotted against longitudinal mode number with circumferential mode number as parameter for a shell possessing dimensional and material characteristics similar to our experimental shell. This mode-frequency diagram was adapted from Arnold and Warburton (Ref. 7) who had presented generalized data for a ratio of shell thickness to mean radius equaling 0. 0525. Our experimental shell corresponded to a ratio of 0. 058 (thickness = 0. 085 in., mean radius = 1. 458 in.), which is not different enough from Arnold and

Warburton's value to justify a tedious recalculation. As a consequence, the numerical values for mode frequencies in Fig. 8 will deviate somewhat from our experimental values, but the general arrangement of the mode frequencies is completely valid.

Consider on the basis of Fig. 8 what will be found if we search upward in frequency for the presence of normal flexural modes. The lowest frequency mode of this type corresponds to the mode designation $m = 1$, $n = 2$ followed by the modes $m = 2$, $n = 2$ and $m = 3$, $n = 2$. These first three modes are cleanly separated in frequency from one another. Continuing upward in frequency, we next encounter $m, n = 1, 3$; $4, 2$; $2, 3$; $3, 3$; and $4, 3$ all rather tightly clustered. At still higher frequencies, the $n = 2$ and $n = 3$ modes become cleanly separated again until the $n = 4$ modes enter the consideration. At this point, another clustering occurs. Thus from a consideration of the theory due to Arnold and Warburton, it becomes clear what to expect experimentally. The three lowest frequency, low-order flexural modes ($m, n = 1, 2$; $2, 2$; $3, 2$) ought to be found to be cleanly separated and then a tightly clustered multimodal behavior should be found. This is precisely what did happen. The interferograms of Figs. 12 and 13 are in the frequency region of the anticipated multimode cluster.

A detailed analysis of these interferograms has not been accomplished but the fringe patterns do not obviously contradict what might be expected for the combination of mode-number values involved. The

acoustic excitation used in our experiments would tend to excite all of the modes in this cluster, perhaps not equally well, but on the other hand the exciting-force distribution within the shell does not obviously favor one mode over another.

In order experimentally to separate the modes in this cluster, one would have to utilize forcing functions matched to each particular mode, both in phase and spatial distribution. Such a procedure was utilized by one of the Authors in a previous experimental program (Ref. 8). The use of a single localized driving point could not, in general, successfully delineate the modes of the cluster because of the combinational consequences of m and n both taking on even and odd values. The magnetic excitation employed for Fig. 12 may have been somewhat selective but similar interference patterns had been observed in this frequency region with acoustic drive. The fact that two frequency regions were found, as depicted by Figs. 12 and 13, suggests that this mode cluster was partially separated into two almost distinct subgroupings. Possibly a recalculation of Fig. 8 using the exact values for our shell and displayed on an enlarged frequency scale might hint at such details.

The multimode behavior, which has just been presented, prompts several observations with respect to studies of shell vibration. Initially, it was considered as an undesirable experimental difficulty. It frustrated attempts to obtain an extended sequence of "classical" low-order mode interferograms, a trouble which was not really expected until

much higher frequencies were obtained. Obviously that initial impression was mistaken. As the problem is now understood, it has other implications. It emphasizes the importance of the spatial distribution of the driving function whether in a real operational mechanical system or a somewhat idealized laboratory apparatus. In the laboratory, neither a point drive or a distributed drive is necessarily the "correct" choice for experimental studies.

A second observation is that some aspects of high-order modal behavior have been encountered experimentally among what are normally considered to be low-order modes. The frequency extent and complexity of this low-order mode clustering are open to experimental manipulation through selection of shell dimensions. For a limited frequency range, the modal density can be controlled so that one works with a small finite number of participating modes rather than with a large number of modes requiring a full-blown statistical approach. Such a situation might facilitate some types of investigation.

A third observation is that for real vibration-engineering studies, it appears likely that the scope of discrete low-order modal behavior is small but not trivial, that the transition to high-order modal behavior progresses typically by mode clustering rather than gradually increasing modal density, and that a fully developed high-order modal behavior is soon encountered unless the driving function introduces strong spatial discrimination.

Let us return to the unsolved experimental difficulties which afflicted the interferograms as we worked toward higher frequencies. In Fig. 12, extra fringes wandered across the shell. They are thought to be caused by thermal expansion as discussed earlier. Although a single photographic reconstruction is unable to reveal it, these extra fringes are not localized in space the same way as the time-average flexural-mode fringes. This point can only be verified by a parallactic examination of the original time-average holograms. The driving power was high and the thermal drift was quite severe.

We discovered later that the voice coils in the drivers had been damaged by overheating. Consequently, little emphasis is placed on trying to make detailed analyses of the fringes beyond the fact that they did occur at the stated frequencies. This region merits reexamination in light of the multimodal behavior with the experimental difficulties suppressed.

Because of the driver failure, Fig. 13 was obtained using magnetic excitation. We wanted to finish the initial examination of these modes without changing the support structure because we had not taken time to investigate if the interferograms could be replicated in detail if the shell structure had to be reassembled. The exact patterns obtained with magnetic excitation were quite dependent upon driver location as would be expected in view of the modal cluster involved. Actually, the behavior evidenced in Figs. 12 and 13 was accompanied by very shrill

radiation judging by ear alone in a moderately reverberant laboratory space.

We did not restudy this frequency region from 2700 Hz to 2900 Hz immediately upon repairing the drivers because of the desire to get on with exploratory studies of a rib-stiffened shell structure. The time needed for a restudy with the unstiffened shell never became available except for visually inspecting the real-time fringes in support of the sound-power measurements discussed in Section 2. 2.

During the sound-power experiments, after several reassemblies of the uniform shell, the higher order mode shown in Fig. 14 was located at 5743. 2 Hz. It is identified as an $m = 5$, $n=4$ mode. The antinodal regions show curious variations in shape, size and orientation. The detailed causes have not been identified, but the flexural wavelengths on the shell are perhaps short enough to be influenced by local anisotropies of the shell material. Also, acoustical normal-mode behavior of the interior cavity might be exerting an influence through the distribution of the driving function. In any event, there are certainly implications with respect to structural engineering and to the distribution of radiation.

A more detailed study of the frequency region around 5740 Hz would be needed for elucidation. Figure 8 certainly does not suggest that this particular mode should be so cleanly delineated with other

modes at nearby frequencies suppressed or missing. This one interferogram merely verifies the possibility of working with discrete higher order flexural modes of cylindrical shells under appropriate conditions of excitation.

2. 1. 2 Rib-Stiffened Shell. The general vibrational behavior of a uniform shell, as revealed by hologram interferometry, correlates reasonably well with the existing body of engineering knowledge about such shells. The mode frequencies fell about as predicted. Amplitude distributions at and near resonances are less perfectly predicted theoretically. In this instance, hologram interferometry clearly displays what did occur on the actual shell. However, a detailed quantitative analysis of the interferograms is needed to extract precise numerical data. This is feasible using the same interferograms presented above but, at this comparatively early stage, we wanted to exploit a more qualitative evaluation of those features which could be comprehended by inspection. Moreover, before attempting sophisticated analysis mode by mode, a tighter control over excitation conditions ought to be exercised.

Thus we shifted attention to stiffening the shell with internal ribs. The point to be determined first was whether or not the presence of a rib would appreciably influence the vibrational behavior of the shell. Furthermore, would any changes in the modes be readily apparent by inspection of the interferograms or would an exacting analysis be needed

to detect the changes? These experiments with ribs constitute a departure from a strictly academic orientation to a more design-engineering orientation of the program. The use of a rib is prototypical of what a design engineer might do to solve a static-deflection problem. Therefore, if one could see and comprehend the dynamic consequences of stiffening a structure with a rib by viewing the appropriate sets of interferograms, a design engineer could rapidly acquire insight into the effects caused by his design changes. On the other hand, if more detailed analyses were needed to display the consequences of such design changes, then hologram interferometry would become, in this application, more of a research tool than a design-engineer's tool. Either approach has real value; it is strictly a matter of learning how to use hologram interferometry most efficaciously.

The original plan was to press or cement various ribs into place within the shell at different spacings and to look for the dynamic consequences. In fact, we became so involved with displaying the effects in detail caused by the first rib and with the subsequent sound-power measurements, that studies with multiple ribs had to be postponed. This change from the original plans was not inappropriate however. As the composite interferograms demonstrate, each vibrational mode studied by hologram interferometry potentially has an enormous amount of detailed information associated with it. Thus it became essential to learn to interpret a more limited but cogent subgroup of information

about detail related to individual modes before attempting to investigate a wide variety of structural changes.

An initial question was where to place the first rib. Figure 15 shows the rib's dimensions and location. It was reasoned that this central location was a rational choice on the following grounds. The preliminary studies on the uniform shell had revealed the modes (m, n = 1, 2; 2, 2; 3, 2) quite clearly while beyond them the situation was confused. In the case of an $m = 1$ mode, a rib should, to first approximation, slightly stiffen the shell. The principal result should be a small increase in the mode frequency and if any significant changes occur in the mode amplitude distribution, the shape of the fringe patterns should reveal them. For an $m = 2$ mode, a central rib probably would have negligible effect because it would be located in a nodal region. In the case of an $m = 3$ mode, a more complicated involvement might be expected. For the central flexure of an $m = 3$ mode, a single rib ought to stiffen the shell much as for an $m = 1$ mode. However, the two outboard loops could only experience the rib by a transfer of its effects through the shell. Because of the radial symmetry of the rib, the values of n should be of small consequence in all three cases discussed above. Therefore, one rib located at the center ought to provide at least three distinctly different structural involvements, all interpretable to some level based on modes already successfully displayed by hologram interferometry on the unstiffened shell. Probably higher order modes would

be detected for the stiffened shell also but interpretation might be difficult because of incomplete comparison data for the uniform shell.

Figure 16 shows a composite of some survey results for the rib-stiffened shell excited acoustically.

Figure 17 shows similar results using an unbiased magnetic exciter located behind the shell on axis and seven inches from the right-hand end.

Figure 18 shows interferogram results of a more comprehensive investigation of the stiffened-shell $m, n = 1, 2$ mode which occurred in the vicinity of 1097 Hz. For the same electrical signal to the acoustic drivers, the stiffened shell shows less amplitude response than for the corresponding mode on the uniform shell. (See Fig. 9 for comparison.) The evidence of mode splitting which is so clear in Fig. 9 has vanished in Fig. 18. The interference pattern now is more elongated with a region in the center where the fringes appear to be nearly straight and parallel. And, of course, the mode frequency has shifted upward by about 60 Hz, or roughly 6 percent, presumably due to a modest increase in effective mode stiffness caused by the rib. The frequency range over which shell motion is large enough to be detected holographically is similar for the stiffened and unstiffened cases.

Figure 19 shows the rib-stiffened results for the mode $(m, n = 2, 2)$ which occurs in the vicinity of 1322 Hz. The frequency shift is small as was anticipated, and it amounts to only about 4 Hz. (See

Fig. 10 for comparison.) Split-mode behavior is clearly displayed in Fig. 19 but the structural changes seem to have eliminated the cusp-shaped fringes which were so prominent in Fig. 10. For the rib-stiffened shell, the lower frequency component of the split mode responds with a much larger amplitude than the higher frequency component, six dark fringes compared with three. This result contrasts with the behavior of the uniform shell in which both components of this split-mode show about equal response. The original centerline (at 90 degrees) in the case of the uniform shell has unavoidably been rotated downward by approximately 25 degrees. Overall, it appears that this particular mode has not been altered in dynamic behavior very much by the presence of a stiffening rib located at its circumferential nodal line.

Figure 20 displays the rib-stiffened results for the mode (m, n = 3, 2) in the vicinity of 1974 Hz. The upward frequency shift for this mode is about 1.6 percent, only about one quarter the percentage shift found previously in the case of the (m, n = 1, 2) mode. The maximum amplitude of response compared with Fig. 11 has been reduced. Likewise, the frequency range over which detectible amplitudes occur has diminished from greater than 19 Hz to less than 12 Hz. The split-mode effects have disappeared or have been reduced to the point where they are not easily recognized. There does seem to be a hint of a nearly constant amplitude fringe pattern which merely rotates upward with increasing frequency. The lateral separation of the two circumferential

nodes appears larger than for the uniform shell but a more detailed fringe analysis would be required for certainty. Finally, the inception and disappearance of the interference fringe patterns with increasing frequency as shown in Fig. 20 are much more symmetrically disposed than in Fig. 11.

Figure 21 displays interferograms of the rib-stiffened shell throughout a frequency range from 2825 Hz to 2884 Hz. Rather complex behavior is evident but near the middle of the range there occurred a clearly discernible (m, n = 4, 2) mode. Audibly, the radiated sound was very shrill.

The frequency range of Fig. 21 is the range where a multiple-mode cluster was expected in the case of a uniform shell and the interferograms for that range (Figs. 12 and 13) displayed a confusing complexity. One would expect that the modes corresponding to m-equal-an-even integer would be scarcely affected by the stiffening rib as located in these experiments. Likewise modes for m-equal-an-odd integer ought to have their frequencies shifted upward and, presumably, the value of n is rather inconsequential. This expected behavior has been largely confirmed for the three lowest frequency modes. Now, referring to the mode cluster shown in Fig. 8, one might expect the (m, n = 1, 3) mode to be shifted upward in frequency as well as the (m, n = 3, 3) mode. On the other hand, the (m, n = 4, 2 and 2, 3) modes should be hardly affected. Thus it is plausible that a relatively clean (m, n = 4, 2) mode

should appear in Fig. 21 and that fringes reminiscent of an (m, n = 2, 3) mode might appear also. Evidently Fig. 21 should be interpreted to the effect that the multiple-mode cluster has been partially separated by the stiffening rib. However, the complexity remaining is far too great to interpret fully without collecting much additional data. The composite effects of multiple modes with some or all of them split modes as well are probably to be found in Fig. 21.

Figure 22 shows the highest frequency range which was examined in detail, namely from 3804 to 3862 Hz. Complete identification of modes is uncertain at this point in time although the three patterns spaced longitudinally argue for an $m = 3$ mode assignment. The outboard interference patterns have an intriguing conformation. The S-shaped dark fringes running from top to bottom of the cylinder must imply a constant value of dot product between the sensitivity vector and the displacement vector. However, this one piece of information does not seem to be a sufficient clue to solve this unknown vibration. A more detailed investigation, possibly with the assistance of a phase-detection technique, is needed to complete the analysis. Notice the abrupt "mirror-image" fringe change between 3812 and 3818 Hz and also the many cusp-shaped fringes. It seems likely that Fig. 22 displays a composite of multiple-mode and split-mode behavior.

Other regions of vibration at higher frequencies, and indeed still others scattered throughout the whole frequency range, could have been

investigated by using a more powerful excitation or a different method of excitation. It was decided, however, to proceed with the related sound-power measurements at this point. Moreover, a spate of laser-operation troubles required the turning of our attention to some non-holographic experiments until laser repairs could be obtained.

2. 2 Sound-Power Studies

Sound-power studies were undertaken to provide correlative information which, in conjunction with hologram interferometry, could provide a basis for engineering decisions. Intuitively, the stiffening rib must cause some alteration of the vibrational behavior of a cylindrical shell. The criterion for deciding whether or not the induced changes are appropriate must come from outside the scope of holographic research. These sound-power studies represent one approach to providing such a criterion for decision.

A single stiffening rib is considered prototypical of the change a design engineer might make. As such, it serves as a vehicle for pursuing the present research program rather than a complete research end in itself. This section therefore describes how the sound-power measurements were accomplished. Then specific results are presented for the uniform shell and for the rib-stiffened shell.

Accurate sound-power measurements are not an especially common type of acoustical measurement although a satisfactory technical

background for them does exist. Each of the vibrational modes of the experimental shell has distinctly different directionality characteristics relating to radiated sound. Therefore, the method of sound-power measurement must accommodate these source characteristics. The sound-power measurements reported here were obtained in a reverberation room and because pure-tone measurements were needed, a rotating reflector vane in the reverberation room was used to provide a time-varying boundary condition.

The principle of sound-power measurement in a reverberation room is based upon the assumption of a diffuse sound field and the existence of a specific relationship between acoustic energy density and sound pressure in such a field. Then, a measurement of the space- and time-averaged sound pressure level in the reverberation room due to steady operation of the unknown sound source is the primary datum. One also needs to know the rate of acoustic energy loss from the reverberation room, given by the decay rate of the sound in the room, as well as certain constants of the system. Such information is needed for each frequency of interest. Under these appropriate conditions, the following equation holds:

$$W = \langle p^2 \rangle \langle D \rangle \left(\frac{V}{10 \rho c^2 \log_{10} e} \right) \left(\frac{1 - e^{-\bar{a}}}{\bar{a}} \right) \qquad (1)$$

where

W is the sound power of the source,

p is the sound pressure in the reverberation room due to the source,

D is the decay rate in the reverberation room,

V is the volume of the reverberation room,

ρ is the density of air,

c is the velocity of propagation of sound,

e is the base of the natural logarithms,

$\bar{a}$ is the average Sabine absorption coefficient for the reverberation room with the source present.

and using

$D = 60/T_{60}$; T_{60} is the reverberation time of the room,

and

$T_{60} = \frac{0.049V}{\bar{a}S}$; Sabine equation for foot units,

S is the surface area of the reverberation room.

The angular brackets surrounding the first two terms indicate that these two quantities are to be averaged over the space in the reverberation room as well as averaged with respect to time. The rotating reflector vane essentially converts the space-averaging requirement of $\langle p^2 \rangle$ into a time average over a time interval relating to the rotational period of the reflector vane. The composite time-average value of the sound pressure p results from the use of a true RMS readout meter,

the meter damping, and any residual averaging done by eye while reading the meter.

The decay rate of the reverberation room is obtained in a separate measurement conducted at the same frequency. In this case, the sound signal ordinarily is produced by a loudspeaker which can be more readily switched on and off than the actual sound source whose power is being measured. Space-averaging during sound decay is accomplished by allowing the rotating vane to carry the microphone with it during the decay-rate measurements. Such measurements are replicated many times with starting points which are randomized with respect to vane position. The time-averaging is accomplished in the rectifier circuits associated with the measurement of the reverberation time T_{60}.

The volume of the room V, of course, is a value easily determined for a rectangular room and is constant for any particular measurement facility. The quantity (ρc^2) relates to the acoustical properties of the air in the reverberation room and, under most laboratory environments, is virtually a constant. It has a negligible temperature coefficient and changes only slightly with atmospheric pressure. Only the Sabine coefficient $\bar{a}$ remains to be considered. It is related to the decay rate D through the Sabine reverberation equation, and this equation in turn includes the volume V and the surface area S of the reverberation room.

If Eq. 1 is cast into logarithmic form and the constants appropriate to our reverberation room evaluated, then we obtain the following expression:

$$L_w = L_p + 10 \log_{10} D - 0.00049D - 10.0 \qquad (2)$$

where

L_w is the sound power level of the source expressed in decibels relative to 1×10^{-12} watt,

L_p is the sound pressure level expressed in decibels relative to 2×10^{-5} newton/meter^2, and

D is the decay rate in dB/second.

(The term 0.00049D is the residual effect of the Sabine absorption coefficient term $\bar{a}$ which is negligible for the conditions of this experiment.)

Of course, L_p has to be measured with a microphone which has been properly calibrated for a diffuse-sound field. Such a calibration can be accomplished directly in a reverberation room using a diffuse-field reciprocity method or it may be obtained by pressure calibration in a coupler in conjunction with a diffuse-field factor calculated from known directionality characteristics. The absolute value of sound power level thus depends critically upon the precision with which the microphone's calibration is determined. Relative values of the sound power level are less demanding and essentially require only a detailed knowledge of the

microphone's frequency characteristics. The condenser microphone was not completely recalibrated for the sound power measurements reported here, but it has an excellent calibration history and there was no reason to expect more than a trivial shift in calibration. Thus a quick check, rather than a laborous full recalibration, was considered sufficient for present purposes.

Figure 23 is a block diagram of the instrumentation used for the sound-power measurements while Appendix C. 2 lists the particular electronic components utilized. The one-third octave band filter was used to improve the signal-to-noise ratio of the acoustic signal, but its use necessitated an independent measurement of insertion loss at each frequency for which data were collected. A separate true RMS audio voltmeter was used for all readings because its decibel scale was uniformly spaced, a feature which aided the eye to average residual meter fluctuations. The decay rates were obtained by averaging two sets of twenty trials and requiring agreement to within two percent; otherwise a third set of twenty trials was taken and entered into a grand average. Previous elaborate statistical studies had indicated that the twenty trial procedure was optimal for our facility.

In order to effect the sound-power measurements, the cylindrical shell was moved from the granite slab in the holography laboratory onto the floor of the reverberation room. In both cases, the centerline of the shell was 8-1/8 inches above the supporting surface, floor or granite

slab. This distance had been selected originally for holographic convenience, and it was used in the reverberation room also to maintain the acoustic near-field as nearly constant as possible. The same excitation instrumentation as shown in Fig. 3 was used with the exception of the oscillator. During the sound-power measurements, the beat-frequency oscillator associated with the decay-rate instrumentation (Fig. 23) was used to excite the shell also.

Chronologically, the sound-power measurements were performed first on the rib-stiffened shell because holography had just been completed on this particular shell configuration. However, the shell's mode shapes and mode frequencies were reverified holographically using visual observation of real-time fringes just prior to moving the shell to the reverberation room. The mode shapes checked as closely as could be discerned by eye, but small frequency shifts of a few hertz were suspected. The rib-stiffened shell was then transferred to the reverberation room and the sound-power measurements taken. Subsequently, this shell was replaced on the holography table and again examined visually using real-time fringes. No obvious change in vibrational behavior could be discerned.

At this point, the shell apparatus was disassembled, the stiffening rib was removed, and the uniform shell was remounted on the drivers. This uniform shell was set up again on the hologram table and examined by the method of real-time fringes to see what changes had

occurred. Recall that in addition to reassembly, the driver units had been repaired since the sets of time-average interferograms shown in Section 2. 1. 2 had been taken. There was a downward rotation of the shell by about 25 degrees, noted earlier, as a consequence of repairing the drivers. The mode shapes for the uniform shell appeared to have been rotated by roughly the same amount now. The general characteristics of mode shape and mode frequency were verified but the mode frequencies seemed to have been shifted upward somewhat. The shell was moved to the reverberation room, the sound-power measurements performed, and then it was replaced for a holographic check.

An accident occurred at this point after completion of the sound-power measurements. Handling stress caused one of the end plugs to slip out of the shell, and the shell apparatus had to be completely reassembled. Subsequent examination with the real-time fringes suggested that small frequency shifts had occurred again but the general mode features were replicated.

Obviously, it would be desirable to know more about the effects of reassembly on the vibrational characteristics, also to design an experimental assembly immune to handling or else to arrange to take the holograms in the reverberation room. We believe, nevertheless, that the sound-power measurements accomplished their primary purpose, that of providing information to correlate with the observations obtained by hologram interferometry. The problems which did arise

were normal experimental difficulties which can be guarded against in future studies.

Two reservations about the interpretation of the sound-power data should be noted. First, there will obviously be some direct radiation of sound energy from the structural surfaces of the acoustic drivers. This source of sound energy was thought to be insignificant in the particular frequency ranges reported here. Nevertheless, this contention ought to be verified by a separate direct experiment.

Second, the use of acoustical excitation makes difficult the determination of how much vibrational energy actually coupled into the shell. It is possible to monitor the electrical energy supplied to the drivers, but the distribution of that energy between the drivers and the shell could not be resolved easily in the present experiment. One concern was that a normal mode of the cylindrical cavity, terminated with unknown end corrections due to the drivers, might fall in the same frequency range as a shell mode and complicate the situation. However, a survey of the current-voltage characteristics of the acoustical drivers reflected no evidence of cavity modes near the shell modes although cavity modes were found at other frequencies.

The ranges of frequencies employed in the sound-power measurements were larger than for holography. These larger ranges were utilized partly because of the frequency shifts which had been noticed since the interferograms were taken, and partly to display the tails of

the sound-power curves at frequencies where the resonant effects would be small. The end points of the frequency ranges were actually selected by observation during the experiments and, by hindsight, were not always the best possible choices.

2. 2. 1 Uniform Shell. Figure 24 presents the sound-power data obtained for the uniform shell in the vicinity of the (m, n = 1, 2) mode. The results are nearly flat with frequency except for a small peak at 1037. 7 Hz which does not correspond precisely with the features found by holography. The weak correspondence between acoustic and holographic measurements may, in this instance, be due to the problems of reassembling the apparatus. The total electrical power supplied to the drivers ordinarily fell in the range of three-to-four watts and so the electro-acoustical efficiency of the system as displayed in Fig. 24 is of the order of 1×10^{-6}.

The sound-power data which corresponds to Fig. 24 is included as Appendix C. 3. It is presented to provide insight into the several numerical values involved. We determined in the course of these experiments that the decay rate of the reverberation room changes only gradually throughout each frequency range. Thus decay-rate data were collected at larger frequency increments than the sound-pressure-level data. However, whenever the decay-rate data showed appreciable change between determinations, or if the sound-pressure levels showed rapid changes in a particular frequency region, additional decay-rate

data were collected at intermediate frequencies.

We believe, without attempting documentation, that these measurements probably are the most detailed sound-power measurements ever undertaken in a reverberation room. Their successful accomplishment depended upon a large amount of research and experience accumulated through the years outside of the scope of this research project. They could not have been reasonably undertaken without that background to draw upon.

Figure 25 shows the sound-power levels found in the vicinity of the (m, n = 2, 2) mode. These results are quite interesting when compared with the corresponding interferograms in Fig. 10. A double peak, with a frequency separation of about two hertz, is cleanly resolved. Allowing for the frequency shift discussed earlier, these two peaks would seem to correlate with the split-mode behavior displayed by the interferograms. The sound-power peaks rise nearly 10 dB above the neighboring frequencies; a result which indicates an increase in radiated sound power by nearly a whole order of magnitude. The orderly progression of data points is indirect evidence of a well-controlled experiment.

Figure 26 presents the sound-power results in the vicinity of the (m, n = 3, 2) mode and is to be compared with the interferograms in Fig. 11. A double peak occurs again, suggesting split-mode behavior. In this case, however, the pattern is less sharply delineated and the

lower frequency peak appears relatively broad. The frequency shift amounts to roughly ten hertz.

Figure 27 presents the sound-power data for the frequency region containing the mode cluster discussed in Section 2. 1. 1. Precise mode identification had not been accomplished for the interferograms in Figs. 12 and 13, but three or four modes may contribute to this cluster. Figure 27 verifies that significant acoustical activity also takes place. A complete interpretation in terms of modal contributions is not possible, however, with the limited data at hand. Future experiments might be aimed at resolving this particular mode cluster.

Finally Fig. 28 presents the sound-power data in the vicinity of the (m, n = 5, 4) mode. (See Fig. 14 also.) An unsymmetrical peak of about 10 dB occurs and the shape of the curve above the peak suggests that there may have been more vibrational activity which was not recognized from examining the real-time fringes. A complete interferometric survey has not been attempted for this mode.

2. 2. 2 Rib-Stiffened Shell. Sound-power experiments were conducted with the rib-stiffened shell and, chronologically, were completed prior to those for the uniform shell. Likewise, an appreciable time elapsed between the detailed interferographic studies and the sound-power experiments. A procedure of reviewing the vibrational behavior with real-time fringes, then conducting the sound-power measurements, and finally rechecking the vibration with real-time fringes was used for

the rib-stiffened shell also. As in the case of the uniform shell, a small amount of frequency shift was apparent but it was difficult to quantify.

Figure 29 shows the sound-power levels for the rib-stiffened shell in the vicinity of the (m, n = 1, 2) mode. The corresponding interferograms are to be found in Fig. 18, and the sound-power data for the uniform shell vibrating in the same mode are shown in Fig. 24. Figure 29 does not show any significant radiation due to resonance. Moreover, if the excitation energy can be considered equal for Figs. 29 and 24, the rib-stiffened shell appears to radiate about 3 dB less sound power. Such a reduction in radiation is certainly consistent with the behavior noted from the corresponding interferograms. Complete validation probably depends, however, on a more controlled excitation technique.

Figure 30 presents the sound-power data for the rib-stiffened (m, n = 2, 2) mode. Comparison with the data in Fig. 25 for the uniform shell confirms that the mode-splitting is larger for the rib-stiffened condition, about 3. 5 Hz compared with 2 Hz. The peak levels for the rib-stiffened case are slightly lower but the differences are not dramatic. At the current state of experience with the behavior of such shells, one should conclude that the rib made no significant change in sound radiation for this mode; some details have changed slightly but nothing of consequence was recognized.

Figure 31 presents the sound-power data for the rib-stiffened shell vibrating in the (m, n = 3, 2) mode. The corresponding data for the

uniform shell is to be found in Fig. 26. Figure 31 suggests that split-mode behavior has disappeared, at least to the extent that a double-peak in the sound-power characteristic was not resolved. This observation is reinforced by the interferograms found in Figs. 11 and 20. In them, for instance, the uniform shell displays four dark fringes which imply a single-peak displacement amplitude in the direction of the sensitivity vector of roughly 23 microinches at certain frequencies. On the other hand, the rib-stiffened shell evidences at most two dark fringes or roughly 11 microinches single-peak displacement amplitude. But the sound-power level of the stiffened shell increased by approximately 2 decibels whereas the interferometric data would imply a 6 decibel decrease. Thus one might make a tentative conclusion that the stiffening rib has acted to increase the radiation efficiency by altering the spatial distributions of amplitude along the shell surface. This presumption, of course, is subject to the limitations about excitation conditions discussed previously.

Figure 32 presents the sound-power data for the rib-stiffened shell in the vicinity of the (m, n = 4, 2) mode. The corresponding data for the uniform shell from Fig. 27 has been superimposed on Fig. 32. The changes are the most dramatic found among the sound-power data. In the case of the rib-stiffened shell, the peak sound-power level is a full 13 dB (20 times) above the peak level for the uniform shell. In general, the levels are much higher across the entire frequency range

investigated for the rib-stiffened shell than for the uniform shell. As discussed earlier, a mode cluster predominates in this frequency range, and the role of the stiffening rib in restructuring this mode cluster is too complex to resolve from the preliminary data. The dramatic increase in radiated sound power seems much too large to be ascribed to a lack of excitation control. If the results can be truly identified as effects of adding a stiffening rib, then profound consequences are implied for sound-control engineering. In any event, a more complete investigation is in order. This one set of experiments only establishes a possibility of large alterations occurring in radiation efficiency with changes in structure in a transition region between low- and high-order modes. The amount of change encountered in this experiment is not necessarily extreme. It raises the possibility of changes in sound power by one or two orders of magnitude. It also suggests possible explanations for anomalous results which have been found occasionally in other noise studies. Definitely, a more complete investigation is needed.

Figure 33 presents the sound-power data for the rib-stiffened shell in a higher frequency range around 3835 Hz. The corresponding interferograms were presented in Fig. 22. There is a broad radiation peak which seems to correlate with the general behavior seen in the interferograms. Since we do not now have a corresponding set of measurements for the uniform shell, and since mode identification remains uncertain for the stiffened shell, no further interpretation will be attempted here.

These exploratory sound-power measurements have served their original purpose. Such detailed measurements can be accomplished in the laboratory for research purposes. A sufficient correlation has been found between the sound-power results and the interferogram results to verify the worth of this broader two-phased investigation, in spite of some evident experimental deficiencies which need attention in future research. In one instance, a very large change in radiated acoustic power was caused by a seemingly small structural change. This observation implies important acoustical engineering consequences and a thorough investigation should be conducted to enable a definitive explanation of it.

3. INTERPRETATION OF TIME-AVERAGE INTERFEROGRAMS

Real-time interferometry, as described in Appendix A, involves the interference between two coherent subject beams. In contrast, time-average interferometry involves the interference of a single subject beam with itself. This section shows how time-average fringes arise and how they are interpreted in vibration analysis.

3.1 The Bessel Relation

In time-average interferograms of subjects in steady-state sinusoidal vibration, the spacing and relative intensities of the fringes result from the Bessel relation as applied to the specific vibration distribution, and the optical arrangement. It will be assumed that a conventional 2-beam holographic arrangement is used, as depicted in Fig. 34, and that the parameters are so constrained as to preserve linearity in the recording-playback process.

On the vibrating subject, V in Fig. 34, consider the point P(x, y, z) which is reflecting light into the hologram along the path PB. The vibration of P causes this light to be phase modulated with optical phase excursion of $\pm\phi_p$ radians, when referred to the fixed phase of the reference beam. Now, on hologram playback, the corresponding point P' on the virtual image will have an intensity dependent upon the time-

average electric field vector of the light wave received from P by the hologram during exposure.

We shall show that this time-average vector may indeed have a value of zero for certain optical phase excursions, giving dark fringes which are essentially black, and that they may be interpreted as contour lines of constant (projected) vibration amplitude.

During the exposure, which is assumed to last for an integral number of periods of the vibration, the electric field vector of the light wave reaching the hologram from point P may be expressed as

$$\bar{e}_p = \bar{E}_o \sin\left\{\omega_o t + \phi_p \sin \omega_1 t + \phi(x, y, z)\right\} \qquad (3)$$

where

$\bar{e}_p$ is the instantaneous value of the electric field vector,

$\bar{E}_o$ is the crest value of the electric field vector,

ω_o is the angular carrier frequency of the laser light,

ϕ_p is the phase excursion due to vibration of P,

ω_1 is the angular vibration frequency, and

$\phi(x, y, z)$ is a time-invariant phase factor determined only by the location of P(x, y, z).

The phase modulated wave represented by Eq. 3 may be expressed as an infinite series, consisting of a carrier wave and two sets of side-bands.

$$\bar{e}_p = \bar{E}_o \left[J_o(\phi_p) \sin \omega_o t + \sum_{n=1}^{\infty} J_n(\phi_p) \left\{ \sin (\omega_o + n\omega_1)t + (-1)^n \sin (\omega_o - n\omega_1)t \right\} \right] \quad (4)$$

where

J_o is the Bessel function of the first kind, and of order zero, denoting the amplitude of the carrier term, while

J_n is the Bessel function of the first kind of integral order n, denoting the amplitudes of the sidebands.

An important feature of the holographic process is that only wavefronts which are coherent with the reference beam are stored in the hologram. In Eq. 4 the carrier term is coherent with the reference beam while the sidebands are not. Thus only the carrier term is stored, while the sidebands merely add their energy to the general bias level of the hologram, and are not preserved as stored wavefronts.

When the hologram is processed, and the virtual image is reconstructed by application of a suitable playback beam, the amplitude of the image point P' will be proportional to $E_o J_o(\phi_p)$. Since the intensity I_p is proportional to the square of this amplitude, we may write

$$I_p = I_{po} J_o^2(\phi_p) \quad (5)$$

where I_{po} is the intensity of the point P on the image which would have occurred for no phase modulation, i. e., no vibration of P.

A plot of I_p / I_{po} vs (ϕ) shows that dark fringes* occur at

$$\phi = 2.405, \quad 5.520, \quad 8.654, \quad 8.654 + n\pi \text{ radians} \tag{6}$$

The bright fringes of successively decreasing intensities reach their maxima for values of ϕ which satisfy $\frac{d}{d\phi} J_o(\phi) = 0$. These are

$$\phi = 0, \quad 3.832, \quad 7.015, \quad 10.173, \quad 10.173 + n\pi \text{ radians} \tag{7}$$

and produce corresponding intensity maxima of

$$I_p / I_{po} = 1.0, \quad 0.1621, \quad 0.0901, \quad 0.0623, \quad 0.0477, \text{ etc.} \tag{8}$$

The brightest fringe or fringes in the reconstructed image of an interferogram are clearly for $\phi = 0$, i. e., no apparent motion of a specific area. Such areas are denoted as optical nodes. They are easily distinguished from other bright fringes being six times as intense as the nearest neighbors. As we shall later see, optical nodes may arise in two ways. They will appear at places where the vibration vector is normal to the sensitivity vector, or where the vibration vector is zero.

The optical phase excursion ϕ of a point on the surface of the vibrating object is therefore directly obtainable by examining the time-average fringes, and interpolating in Eq. 6 or 7 above. For vibration

*See Appendix C. 4 for tabulated values of vibration amplitude versus fringe count.

analysis, we now need the relation between this phase excursion and its corresponding vibration amplitude. This is discussed in the following section.

3. 2 The Sensitivity Vector $\overline{S}$

This section shows a simple method of finding the phase excursion ϕ_p from the known vibration vector $\overline{U}$ of the point P, and from the geometry of the holographic apparatus. It also illustrates that in many cases this geometry may be arranged to simplify the analysis.

It is assumed that the vibrating point P, in Fig. 34, is in a steady state of simple harmonic motion denoted by the vector

$$\overline{u}(t) = \overline{U} \sin \omega t \tag{9}$$

We now postulate a sensitivity vector $\overline{S}$, such that the scalar product

$$\overline{U} \cdot \overline{S} = \phi_p \tag{10}$$

By simple geometry it can be shown that the maximum sensitivity direction is along the bisector of APB, i. e., the line PS in Fig. 34. Therefore, this is the vector direction of $\overline{S}$. Noting that any component of motion along the line PS will result in a change in both the path AP and the path PB, we can now find the proper value for the magnitude of $\overline{S}$ in Eq. 10 to give the phase excursion in radians. This magnitude is found to be

$$|S| = (4\pi/\lambda) \cos \alpha \tag{11}$$

where α is just half the angle APB, and λ is the wavelength of the laser light.

Another form of Eq. 10 which is sometimes useful is

$$\phi_p = (4\pi/\lambda) |U| \cos \theta \cos \alpha \tag{12}$$

where $|U|$ is the absolute value of the vibration vector, and θ is the angle between it and the sensitivity vector PS.

The sensitivity vector concept may be exploited to arrange the holographic apparatus in a way which simplifies the analysis. As an example, consider the following problem.

Determine the vibration distribution of a flat metal plate in which only the normal components of vibration are desired. Ideally one would then desire a sensitivity vector which was everywhere normal to the surface. When using a simple point illumination source, as in Fig. 34, this can be only approximated. However the approximation is good if we arrange a sensitivity vector which is normal at the center of the plate. This is done by placing a small, flat mirror against the center of the plate, and adjusting the plate's angle until the reflected ray PB is centered on the hologram plate holder. Since rays AP and PB both make equal angles with the normal to the mirror surface, and also to the plate, the sensitivity vector (bisector of the angle APB) is then normal, and the adjustment is complete.

It is true that the sensitivity vector departs from normal at the plate edges, but if this is a small angular departure, one can substitute unity for cos θ in Eq. 12 with little error. This arrangement is then nearly ideal for solving the problem as stated.

3.3 Resolution of Ambiguities

From what has been stated above, it is clear that a known vibration distribution leads in a deterministic way to a specific interferogram fringe pattern. However, the converse is not true. A given interferogram fringe pattern does not lead directly to a specific solution of the vibration distribution but contains ambiguities. It will be the purpose of this section to show how such ambiguities arise, and how they may be resolved.

The general problem may be stated as follows:

> Given a vibrating body of unknown vibration distribution, find the magnitude and direction of vibration vector $\overline{U}$ at point P.

If the body is in sinusoidal steady-state vibration with the motion of surface points being rectilinear, this problem can be solved holographically in no more than four essentially identical steps. In each step a time-average hologram is made, and it will be assumed that at least one optical node (Section 3.1) occurs in each.

Step 1. From hologram 1, the reconstructed image yields a fringe pattern. By a suitable fringe count from an optical node to P, and by interpolation in Eq. 6 or 7 one can compute ϕ_p. Now the value of $|U| \cos \theta$ is found from Eq. 12. Let U denote the tip of the vector $\overline{PU}$ to remind us that it is drawn outward from P, but in an unknown direction. Although neither the magnitude nor the direction of $\overline{PU}$ is yet known, it is still possible to construct a pair of planes K_1 and K_2 which are the loci of point U. These planes are constructed normal to the sensitivity vector $\overline{S}_1$ and are spaced a distance $\pm |U| \cos \theta$ from P. It is now clear that U is located somewhere on either K_1 or K_2.

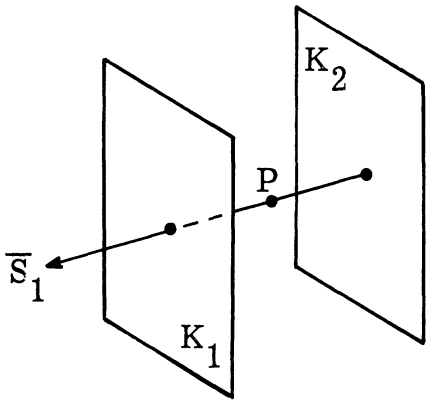

Step 2. Before taking the second hologram, a change is made such that a new sensitivity vector $\overline{S}_2$ at P is located in quite a different spatial direction. By repeating the process outlined in Step 1, two new planes L_1 and L_2 are constructed. Since one of these also contains point U, the latter is constrained to lie on one of four parallel lines. These four lines are the intersections of the two pairs of planes.

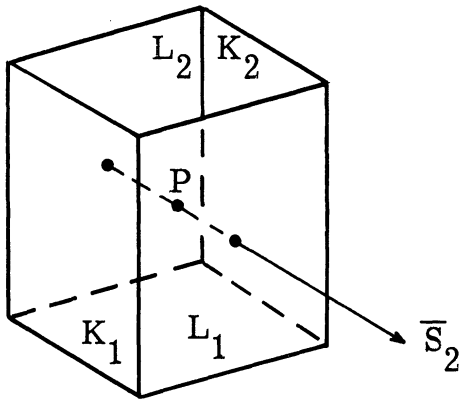

Step 3. Before taking the third hologram, a new $\overline{S}_3$ vector direction for P is arranged which is non-coplanar with $\overline{S}_1$ and $\overline{S}_2$. By repeating Step 1, two new planes M_1 and M_2 may be constructed. These intersect the four parallel lines found in Step 2, producing eight points. The point U must be located at one of these eight points. These form the vertices of a six-sided parallelepiped having geometric center P, which is also the intersection of the four long diagonals.

Note that in this step the ambiguity in magnitude and direction of $\overline{PU}$ has been reduced from an infinite number of values to a finite number, namely eight.

Step 4. The process is again repeated with a new $\overline{S}_4$ vector, (non-coplanar with any previous pair of $\overline{S}$ vectors). Again, two new planes, N_1 and N_2, are found. These two new planes will touch only two of the eight points found in Step 3. This chosen pair of points, which we now designate as U_1 and U_2, will be found on the ends of one of the four long diagonals of the parallelepiped.

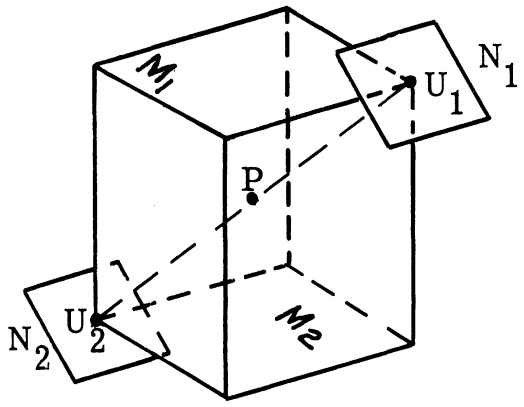

The ambiguity has now been resolved to one in two. These two possible vectors $\overline{PU}_1$ and $\overline{PU}_2$ are equal and opposite. Hence the magnitude and direction of $\overline{PU}$ is established, with a phase ambiguity of 0 or π. A resolution of this final ambiguity is not possible with time-average interferograms since the phase of the vibration is lost in the time-averaging process.

Simplifications:

1. By judicial optical arrangements, as noted in the previous section, one may eliminate one or more steps in the process.

2. If the hologram is large enough, two or more reconstructions may be made, using different viewing directions, from the single hologram.

3. Mirrors may be used to take several views of the subject in a single hologram.

4. In most cases, some prior knowledge of the vibration distribution and vector direction may be employed to reduce the work and thus simplify the analysis.

3. 4 Single-Mode Vibrations of the Cylinder

The previous section dealt with interferograms of vibrating bodies for which there was no prior knowledge of the vibration distribution, resulting in complex analysis procedures. In dealing with the cylinder, advantage is taken of

(a) prior analysis of cylinder vibrations, and

(b) a holographic arrangement based on the above to simplify analysis.

In a single vibration mode, a general point (x,Φ) on the end-supported cylinder may undergo a motion having axial, circumferential and radial components, which may be expressed in the form

$$\left.\begin{aligned} \Delta x &= \bar{X} \cos \frac{m\pi x}{L} \cdot \cos n\Phi \cos \omega t \\ \Delta y &= \bar{Y} \sin \frac{m\pi x}{L} \cdot \sin n\Phi \cos \omega t \\ \Delta z &= \bar{Z} \sin \frac{m\pi x}{L} \cdot \cos n\Phi \cos \omega t \end{aligned}\right\} \qquad (13)$$

where

Δx, Δy, and Δz represent instantaneous values of the axial, circumferential and radial displacements of a point (x,Φ) on the cylindrical surface,

$\bar{X}$, $\bar{Y}$, and $\bar{Z}$ are peak displacement values of the corresponding components wherever they occur,

m and n are the axial and circumferential mode numbers,

x is the distance from one end of the cylinder,

L is the cylinder length,

Φ is the circumferential angle measured counterclockwise from a radial antinode, and

ω is the angular vibration frequency.

The current study of cylinder vibrations includes only those modes where the radial component predominates. In the end-supported cylinder, the ratio of circumferential to radial vector amplitudes is given approximately by $1/n$, while the axial to radial ratio is generally less than 0.1. The radial component is of course of greater acoustical importance, and one would therefore like to examine this component exclusively.

An ideal arrangement for such a study would be to arrange for the interferogram to have equal sensitivity over the visible surface of the cylinder to the radial component and to have zero sensitivity to the two other components. To do this one requires an optical arrangement wherein the sensitivity vector is normal or nearly normal to the surface of the cylinder at least over most of its visible portion.

A study was therefore made of several optical arrangements which would accomplish this normalcy of the sensitivity vector. These methods involve the use of specially shaped optical surfaces to produce the required ray directions of illumination. It is indeed unfortunate that the expense and complexity of such optical arrangements precluded their use under the present contract, however, they could be applied when future demand for specialized analysis justifies the cost.

For analysis of the long (24-inch) cylinder, a compromise arrangement was used. The plan view of the arrangement is shown again in Fig. 35 (a). The subject beam source point A, and the viewing point B (located behind the hologram H) are disposed approximately equidistant from the line of symmetry CL_2 which is perpendicular to the long axis CL_1 of cylinder C at its midpoint P_2. With this arrangement, the direction of the sensitivity vector (the bisector of APB) changes for various points along a central meridian of the cylinder. Typical sensitivity vectors are indicated by P_1S_1, P_2S_2 and P_3S_3. The first and third of these vectors show departures from the ideal condition of being normal to the surface. However in the actual equipment setup, these departures were both less than 15 degrees.

Let us now examine the enlarged elevation view of the cylinder shown in Fig. 35 (b). A typical point P on the outside surface of the cylinder is located at an angular distance Φ_1 from the horizontal plane OP_2. The vector PV represents the vibration of P having circumferential and radial components PY and PZ respectively. The interferogram sensitivity to this vibration is indicated by the projection PW of the vibration vector PV upon the nearly horizontal sensitivity vector PS. It departs from the horizontal in our setup by less than two degrees from top to bottom of the cylinder.

By a suitable fringe count, (Appendix C. 4) the vibration of P inferred from the interferogram is just the vector PW. To deduce the

radial component PZ, one has recourse to the following:

(a) If P is in the near vicinity of P_2, then $PZ \cong PW$.

(b) If P is on or very near a radial antinode, then $PY \cong 0$, and

$$PZ = \frac{PW}{\cos(\Phi_1 + \beta)} \tag{14}$$

where β is the small angle between PS and the horizontal.

(c) If the angle Φ_2 is nonzero, its value may be found by

$$-\Phi_2 = \tan^{-1}(PY/PZ) = \tan^{-1}(k \tan n\Phi) \tag{15}$$

where n is the circumferential mode number, k is a constant to be discussed, and Φ is measured counterclockwise around the cylinder from the center of the radial antinode nearest P_2. The radial component PZ is now given by

$$PZ = \frac{PW \cos \Phi_2}{\cos(\Phi_2 + \Phi_1 + \beta)} \tag{16}$$

The constant k in Eq. 15 is the ratio $\overline{Y}/\overline{Z}$ in Eq. 13. A rather complicated expression for this ratio in the case of the end-supported vibrating cylinder is given in Appendix 3 of an article by Arnold and Warburton (Ref. 7). In the case of long cylinders with small values of m, k is approximately equal to 1/n.

Because this approximation is not exact, and because of the difficulties of measuring the angles Φ and Φ_1, method (c) leaves something to be desired, particularly where an exact analysis is needed. In this case, the better solution is to revert back to the previous section where ambiguity of analysis may be removed by the use of one or more extra holograms, or by the use of a mirror so that two views of the cylinder are seen in the same hologram at the same time. By judicious placement of the mirror, the sensitivity vector will have an angle change between the two views which is best suited to remove the ambiguities in a particular vibrational mode. See, for instance, Fig. 5.

Before leaving this section on simple vibrations of the cylinder, comment should be made about the apparent displacement of nodal points in interferograms. It will be recalled that the brightest regions of interferograms, called optical nodes, are due either to no motion, or to motion normal to the sensitivity vector $\overline{S}$.

Figure 36 shows the section of a cylinder when vibrating in the n = 4 mode. Surface motion vectors were computed by vector addition of radial and circumferential components as derived from Eq. 13, and are shown at the left. Their horizontal projections are shown on the right. (These denote projections upon the sensitivity vector which is here assumed to be horizontal everywhere.) The letters RA, RN and ON denote radial antinodes, radial nodes and optical nodes, the latter occurring wherever the motion vector is vertical, i. e., normal to $\overline{S}$.

This figure illustrates that although five radial antinodes RA occur on the right half of the cylindrical surface, those at the extremes do not render in the interferogram since the projected motion is zero there. In addition, the radial nodes RN do not coincide with the optical nodes ON. The latter are displaced outward with respect to the radial nodes. The outward displacement is zero on the midplane, and increases with distance away from this plane. This outward displacement may become quite large, particularly for small values of n.

On the contrary, there is very little displacement of the projected maxima away from the radial antinodes RA. This convenient result permits relatively accurate location of the radial antinodes, so long as they are not too far from the midplane.

3.5 Split Modes

Due to slight material or dimensional irregularities in the otherwise regular cylindrical shell structure, it is fairly common to find a double-peaked resonance. The two resonant peaks are usually quite close in frequency, and at either peak the mode numbers m and n are the same. This is termed a split mode, and we extend the term to include situations where the resonant peaks are not completely resolved. Although the vibrational distribution is essentially the same for both members of the split mode, a shift in circumferential nodal positions occurs in going from one member to the other. If we denote the members as A and B, and their natural resonant frequencies as ω_A and

ω_B, then the radial antinodes of A when excited alone at ω_A commonly coincide with the radial nodes of B when excited alone at ω_B. It is thus relatively simple to excite either one or the other member alone by proper disposition of the driving force.

When excitation couples to both members, as was found with our acoustic drive, the steady-state response, although always at the drive frequency ω, will consist of components due to A and B with different phases determined by the detuning, $\omega - \omega_A$ and $\omega - \omega_B$, and the quality factors Q_A and Q_B. When $\omega_A < \omega < \omega_B$, the leading and lagging phase responses of these components result in elliptic motion of the surface points on the cylinder. Then the interferogram denotes a vibration amplitude given by the maximum projection of the ellipse on the $\overline{S}$ vector.

As the driving frequency is slowly increased through the region of interest, a double-peaked response is obtained as in Fig. 9. The two peaks may be quite unequal in amplitude as in Fig. 19. In this case the inequality is probably due to a difference between Q_A and Q_B.

When the resonant peaks are quite close together, they are frequently not resolved in the composite interferogram. In such cases the split mode is evidenced by slow rolling of the antinodes as in Fig. 20.

A comprehensive treatment of split modes is beyond the scope of this report, but one special case is worthy of comment. This is called the Quadrature Split Mode.

Quadrature Split Mode

If the resonant peaks are properly spaced, and the driving frequency is at the proper point between them, lower frequency member A will lag 45 degrees while at the same time higher frequency member B will lead 45 degrees. The required conditions are as follows:

$$\left.\begin{aligned} \frac{\omega - \omega_A}{\omega_A} &= \frac{1}{2Q_A} \\ \text{and} \qquad & \\ \frac{\omega_B - \omega}{\omega_B} &= \frac{1}{2Q_B} \end{aligned}\right\} \qquad (17)$$

This situation is called a quadrature split mode, since the responses of members A and B are in time quadrature.

As noted above, the antinodes of A commonly fall upon the radial nodes of B, giving space quadrature as well to the vibrational components. This situation describes a travelling wave which runs circumferentially around the cylinder at angular velocity ω/n. In this case a time-average interferogram does not necessarily reveal the mode number n, but discloses a circumferential band of disturbance, usually of varying amplitude. This is a possible explanation for three of the interferograms in Fig. 7 at 1857, 2906 and 5612 Hz.

3.6 Multiple Modes

When a number of natural vibration modes occur at approximately the same frequency, as illustrated by the cluster in Fig. 8, it may not always be possible to resolve them by appropriate disposition of a point drive. A cylinder may therefore exhibit multimodal response to a single driving frequency. However, it must be recalled that under steady-state driving conditions, there will be only one response frequency, namely at the drive frequency. Therefore the relative response of any particular mode in the cluster is a function of its Q value and the amount of detuning from its natural resonance.

At a given drive frequency, one mode will generally predominate over the others. The interferogram will show this by a vibration distribution pattern which is disturbed from the usual symmetry, the disturbance being due, of course, to the presence of other modes. This may appear as a shift in position, shape or amplitude of the antinodal regions, or a combination of these, producing a variety of results.

An interesting case of multiple mode behavior is found when the predominant mode is also a split mode. As the drive frequency is slowly increased, this predominant mode rolls between its two preferred positions, and the asymmetries may show inversions or reversals. A typical result is shown in Fig. 22.

The variety of results suggested by the above indicates a complex type of behavior which is more common at higher frequencies. It must,

however, be noted that the interferograms are still just as interpretable in so far as they describe the actual amplitude distribution patterns, provided that single frequency steady-state sinusoidal motion is involved.

Cylinder behavior analysis and consequent interferogram interpretation under multifrequency drive (such as narrow-band noise) are beyond the scope of this report.

4. CONCLUSIONS AND RECOMMENDATIONS

The conclusions derived from this research activity fall into two distinct categories, those of general scope, and those specific to the cylindrical shell. The general conclusions are as follows:

1. Techniques have been successfully developed and refined for conducting vibration-analysis studies using real-time and time-average hologram interferometry.

2. The new concepts of the optical isophase surface and the sensitivity vector have aided the understanding and quantitative interpretation of time-average interferograms. These concepts also permit a more intelligent arrangement of the holographic apparatus for specific purposes.

3. It has been shown how ambiguities arise in the interpretation of a single interferogram of a vibrating object. A detailed procedure has been presented which is adequate for resolving these ambiguities in the case of rectilinear vibratory motions of surface points. Further, the procedure may be simplified in specific cases, particularly when some prior knowledge of the vibration is available.

4. In vibration analysis, the value of interferometric data is enhanced by correlation with other independent information. In noise-reduction engineering, the correlation with acoustic data is clearly

desirable. The present work shows how to conduct such an engineering systems study by combining interferometry with sound-power measurements.

Conclusions specific to the cylindrical shell are as follows:

5. The interferometric study of vibrational modes of the cylindrical shell has its greatest value in portraying unusual or unexpected behavior with startling clarity. By far the most unusual result was found in the $m,n = 4,2$ mode. Here, the addition of the central stiffening rib produced a highly developed vibration pattern which was correlated with a 13-decibel increase in radiated sound power. This dramatic increase was observed in only one mode, and one in which the rib coincides with a nodal line. The important conclusion to be drawn is that completely unexpected results, often encountered in vibration-design engineering have been opened to systematic investigation.

6. Both regular and irregular vibrational mode patterns were observed in the interferograms. The regular modes are easily explained by extensions of the single-mode theory. Of particular interest are the sequences of interferograms taken at small frequency increments. Several of these illustrate clearly the shifting split-mode behavior which was expected from theory. The irregular modes were found in frequency regions where the Arnold and Warburton (Ref. 7) mode analysis indicated the presence of a mode cluster. These irregular distributions are therefore interpreted as multiple-mode responses.

7. Apart from the unusual behavior of the 4, 2 mode noted above, the addition of the central stiffening rib made little change in the appearance of vibration distribution patterns. As expected, the resonant frequency increased when the rib was added for modes having odd values of m, but was affected only slightly for modes with even values where a nodal region coincides with the rib.

8. In the case of the widely separated, low-order modes, the interferometric results correlated well with the sound-power data. The split-mode behavior found holographically gave corresponding double peaks of sound power which were clearly resolved.

We make the following recommendations regarding further studies:

1. Apply the methods already developed to a more comprehensive investigation of the acoustical consequences of stiffening ribs and other engineering departures from uniform shells. The large increase in radiated power in the $m, n = 4, 2$ mode has demonstrated the need for a more complete understanding.

2. Investigate ways of applying hologram interferometry in the region of higher order modes where many of the practical noise-reduction engineering problems lie. Such a study may involve development of interferometry with greater sensitivity to small displacements, and concurrently, may involve studies with differently proportioned shells having their higher order modes excitable in large enough

amplitudes for examination by present techniques.

3. Investigate possible methods for sensing the relative phases of antinodes using optical methods compatible with hologram interferometry. The present time-average method obliterates phase information which is important in the study of split-mode and multiple-mode behavior.

4. Investigate advanced techniques of hologram interferometry for vibration analysis with a view to relaxing the present constraints of single-frequency, steady-state sinusoidal excitation currently used with time-average interferometry. For example, it would be useful to examine the response to narrow-band-noise excitation.

In summary, future research should further exploit established techniques and develop new ones to advance our knowledge of the dynamics of engineering structures, and should expand the scope of vibration phenomena which may be examined by hologram interferometry.

5. FIGURES

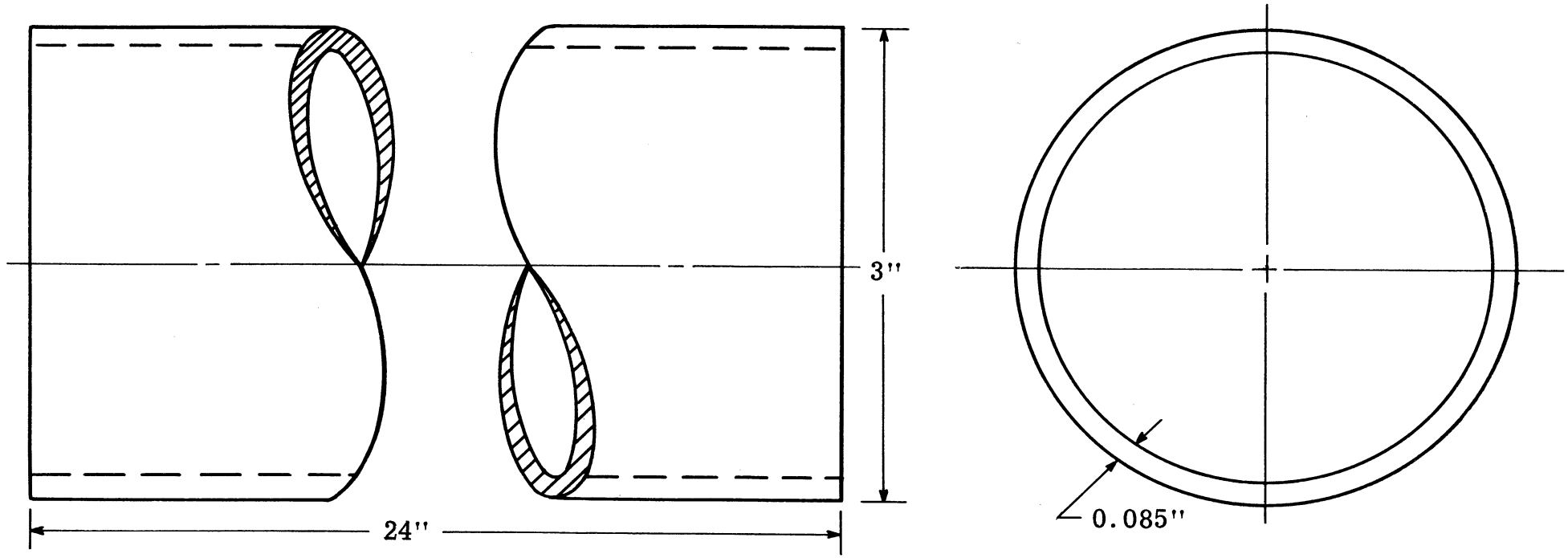

Material: steel tubing

Fig. 1. Dimensions of uniform cylincrical steel shell

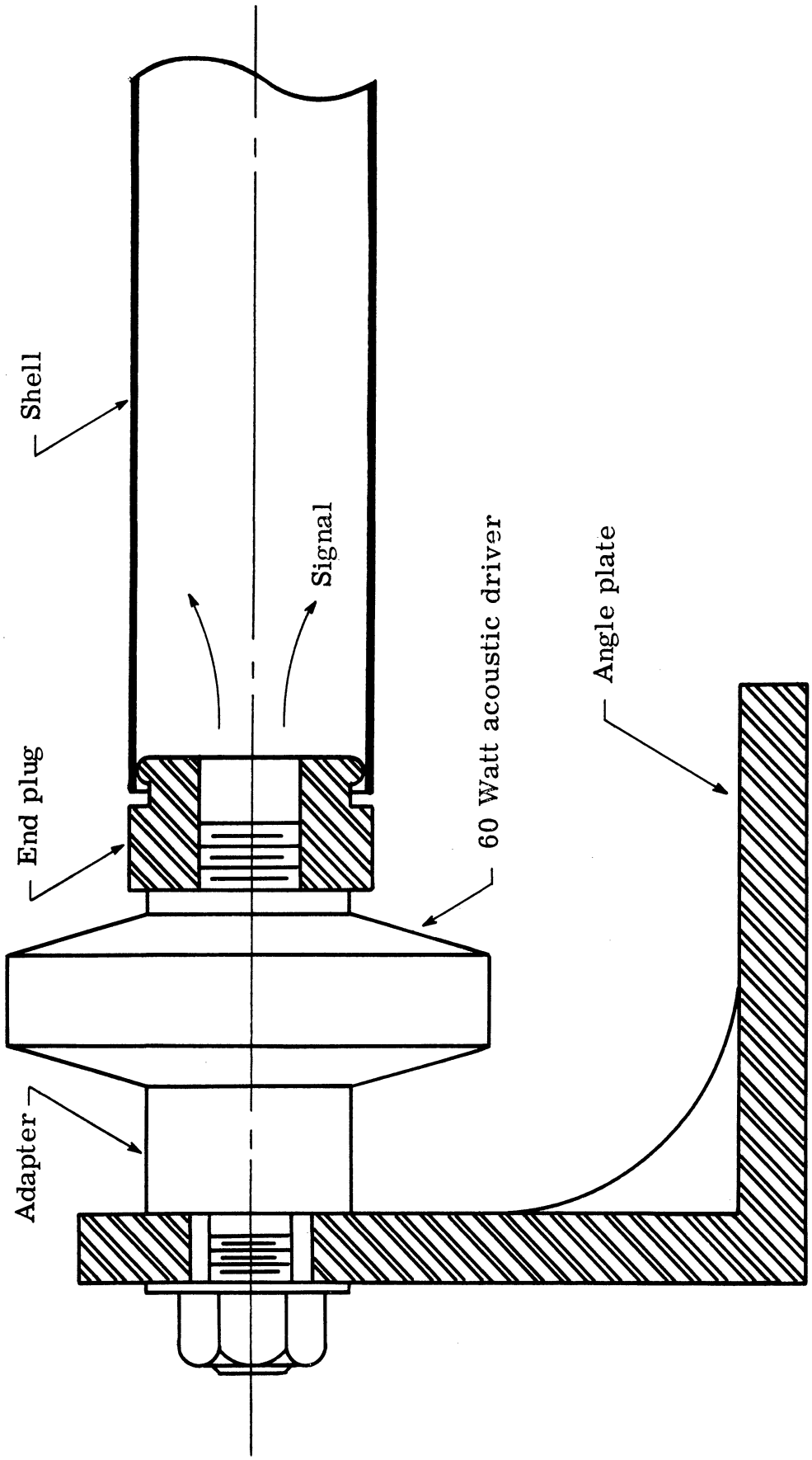

Fig. 2. End support arrangement for cylindrical shell

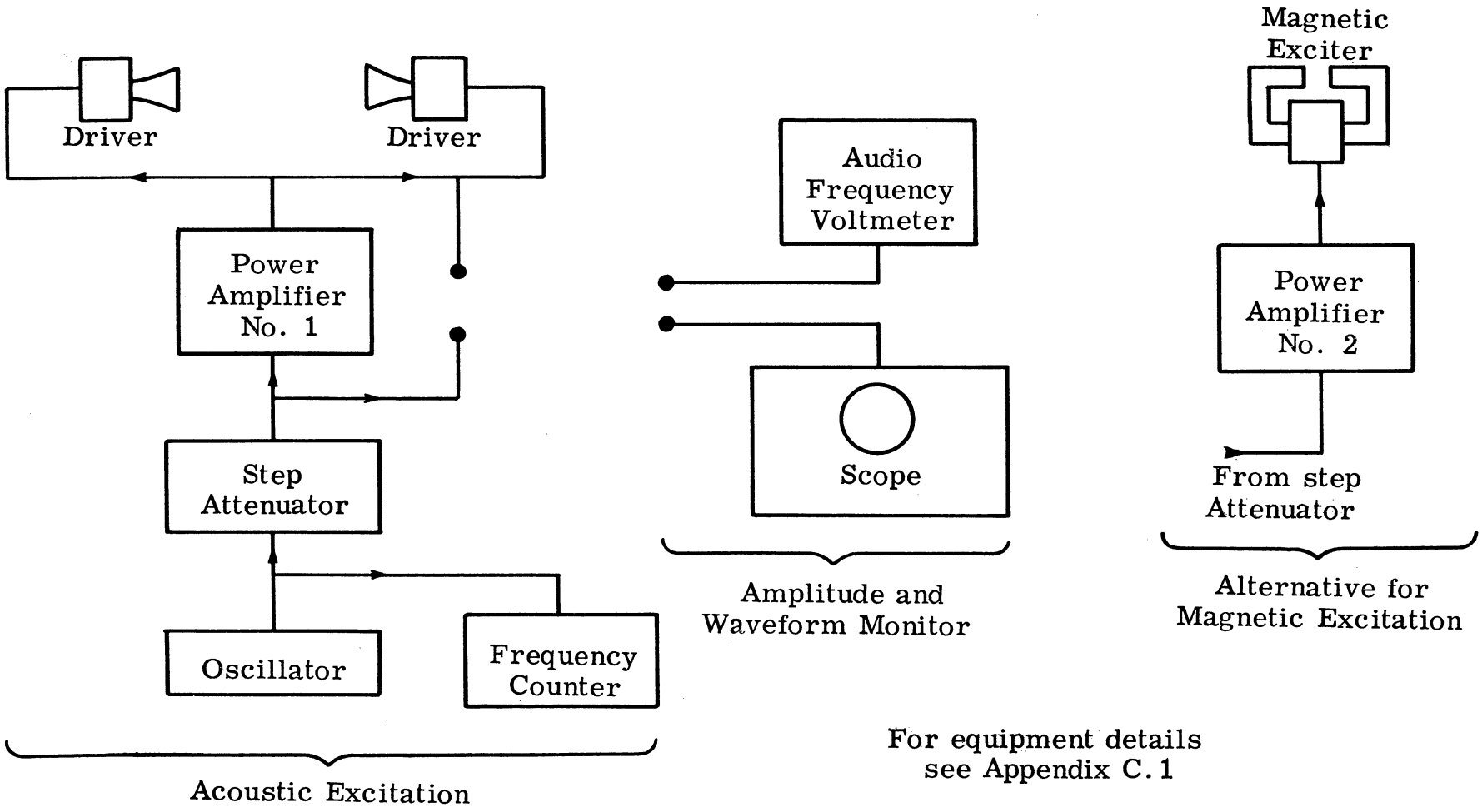

Fig. 3. Block diagram of excitation instrumentation

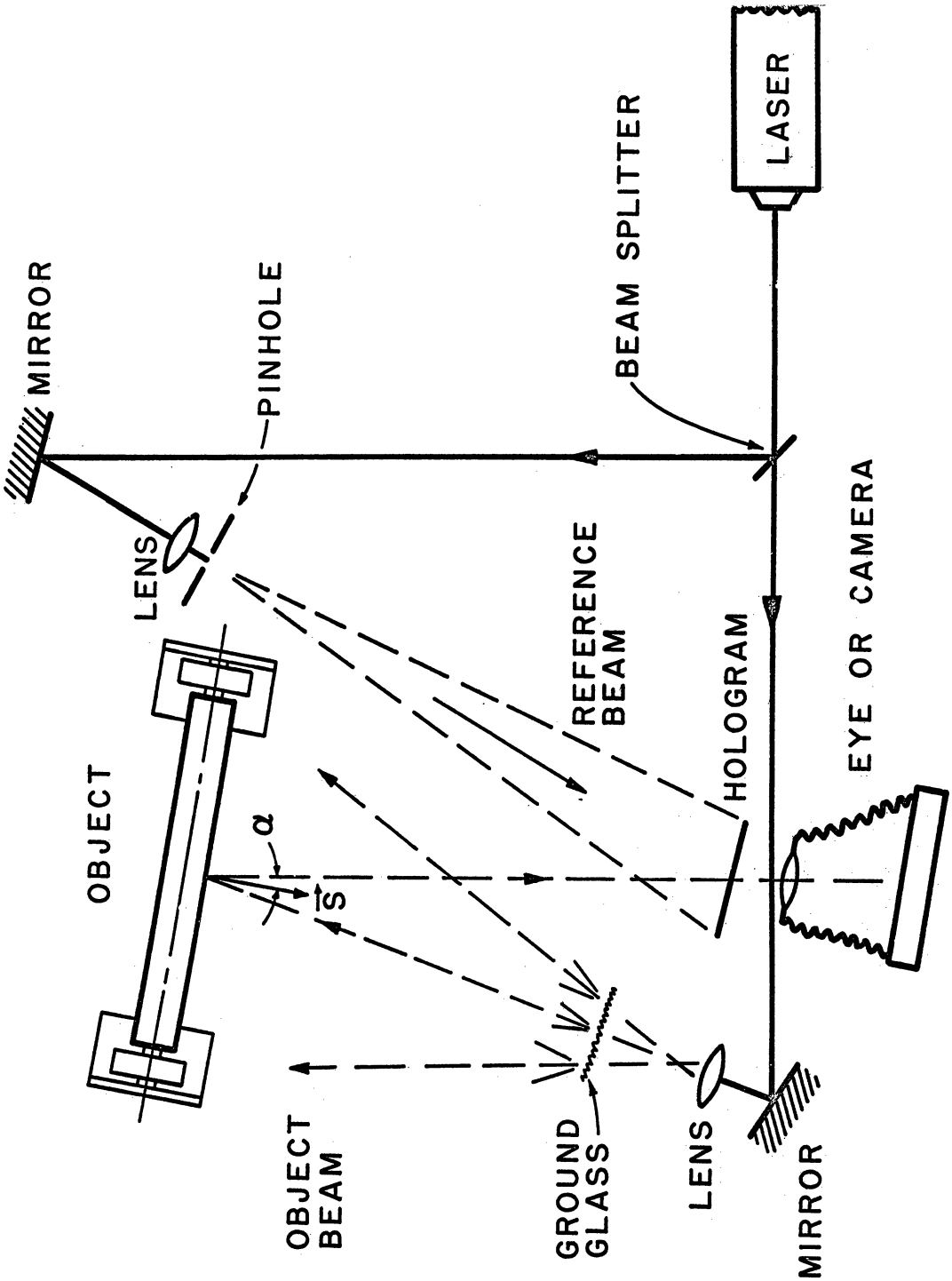

Fig. 4. Plan view of holographic setup

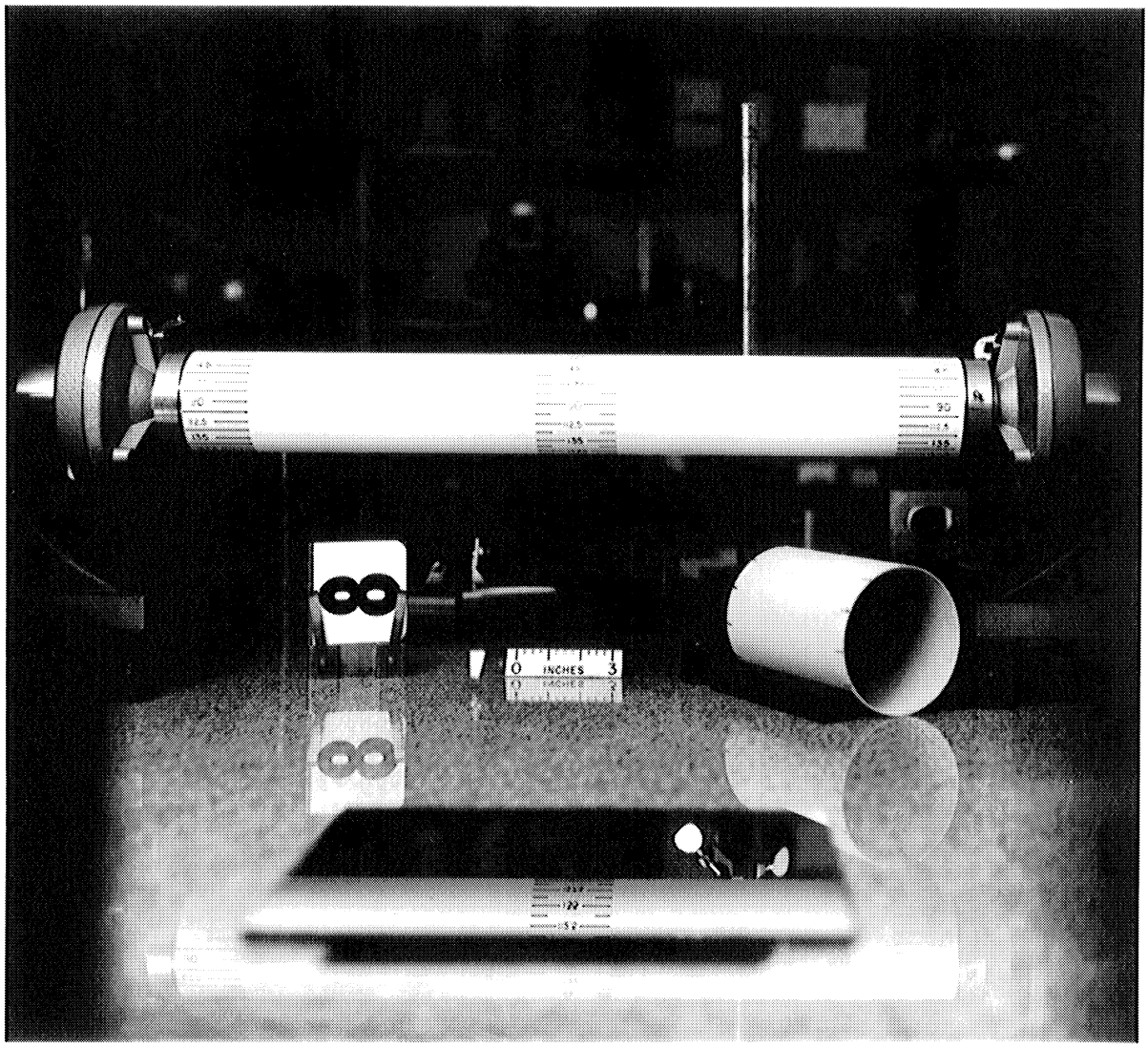

Fig. 5. Photograph of cylindrical shell taken in white light from standard camera position

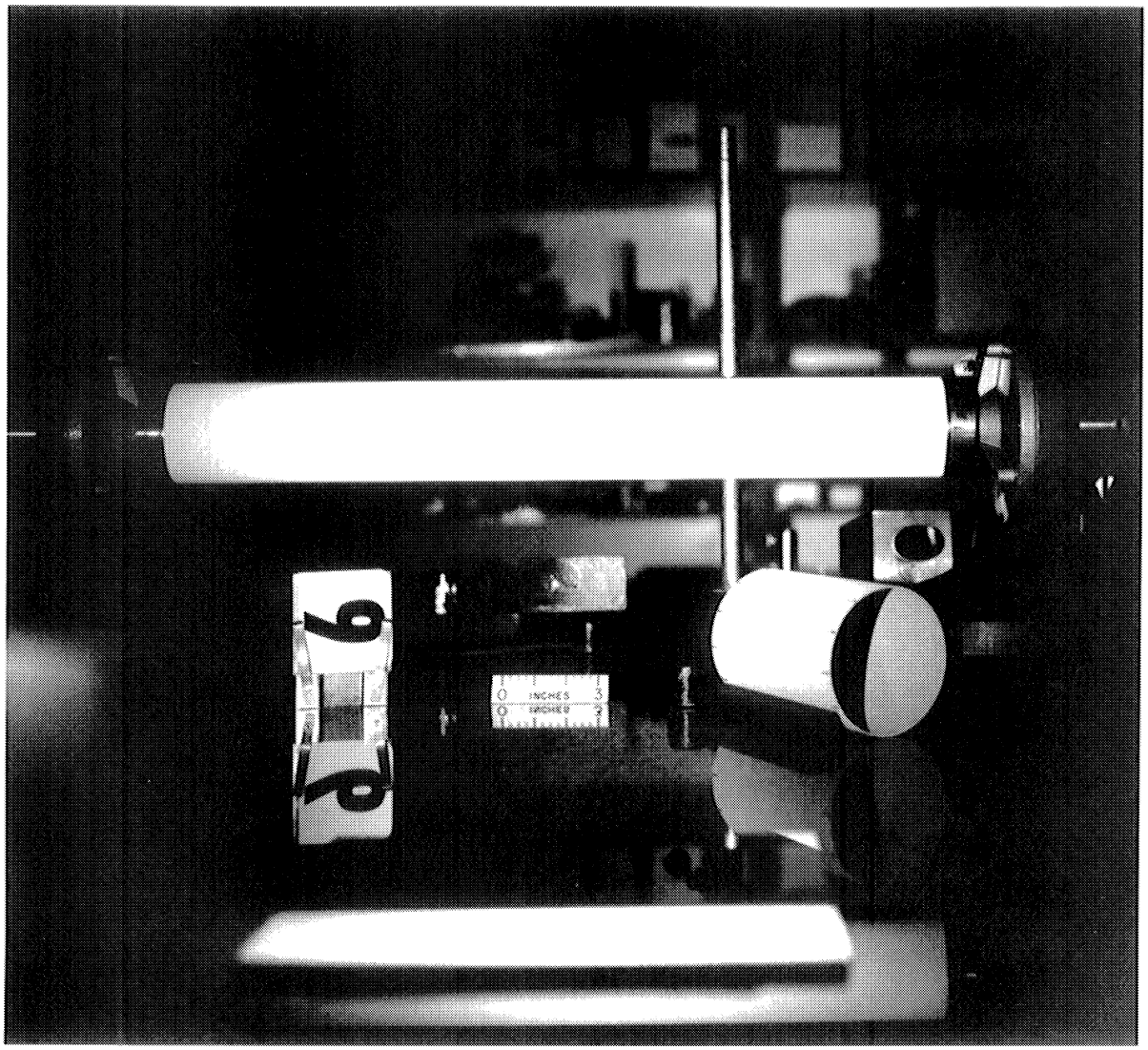

Fig. 6. Photograph of cylindrical shell taken to show distribution of illumination from laser (direct photograph, not a reconstruction)

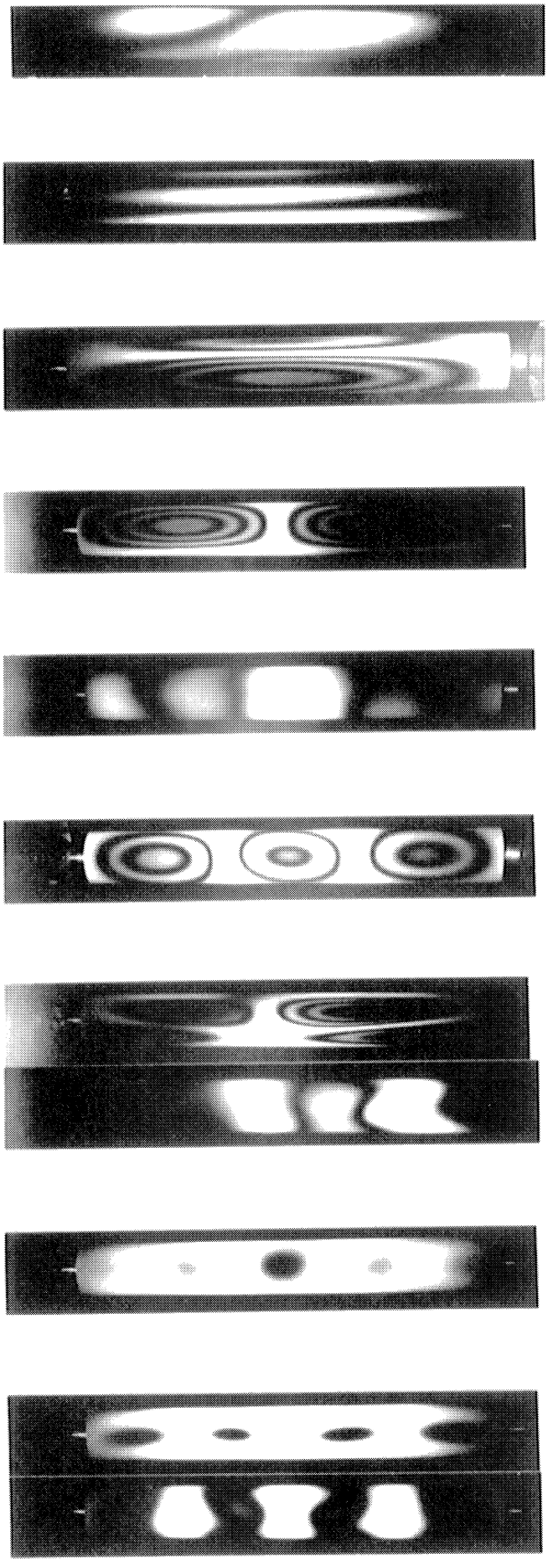

Fig. 7. Composite interferogram of mode survey of uniform shell; acoustic excitation

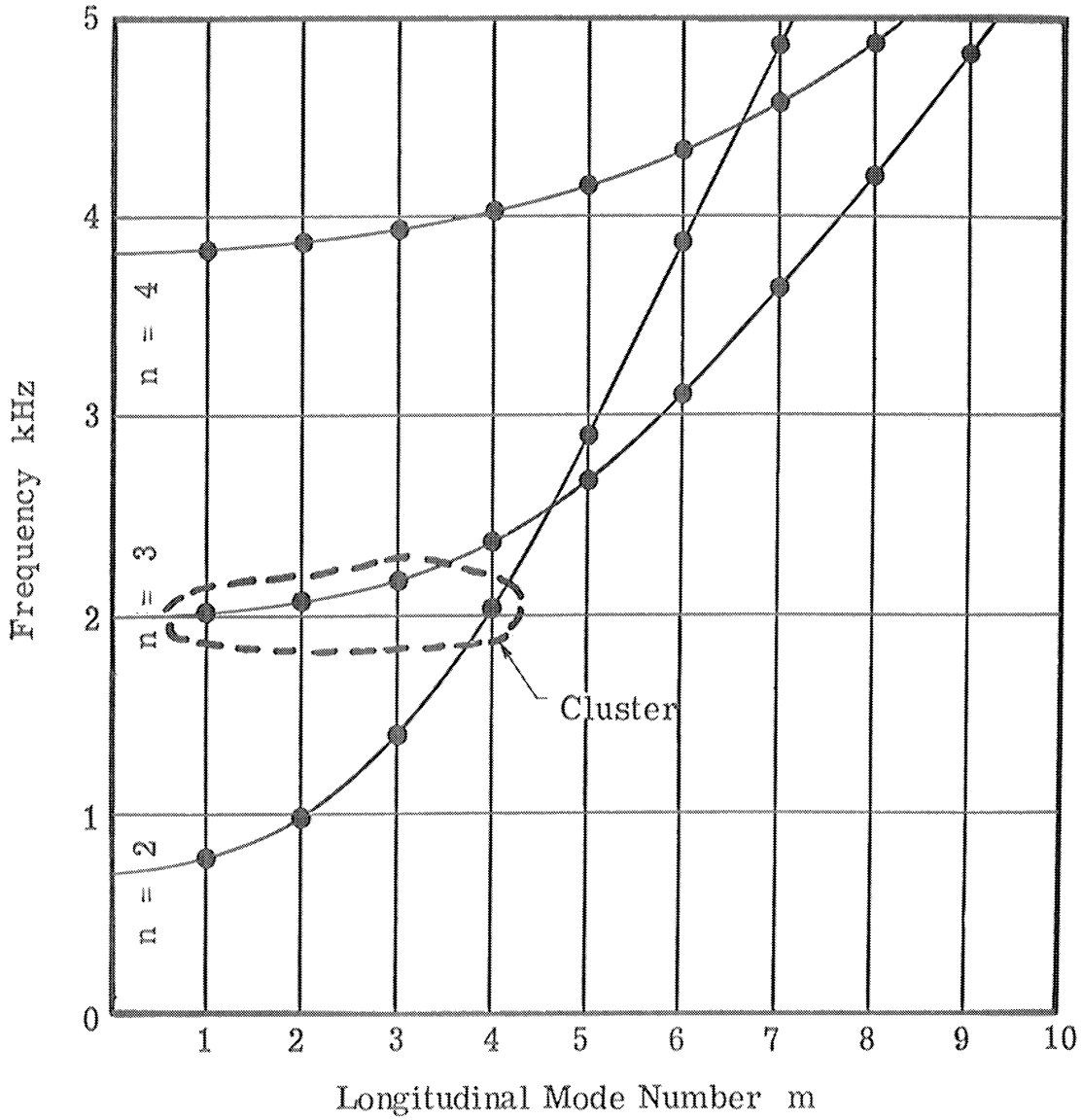

Fig. 8. Mode-frequency diagram for end-supported cylincrical shell after Arnold and Warburton

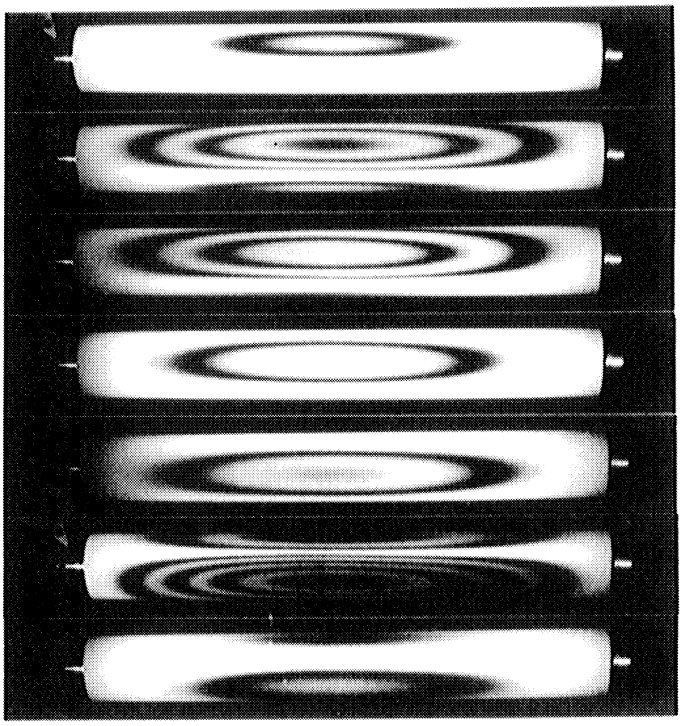

Fig. 9. Composite interferogram for uniform shell; m, n = 1, 2 mode

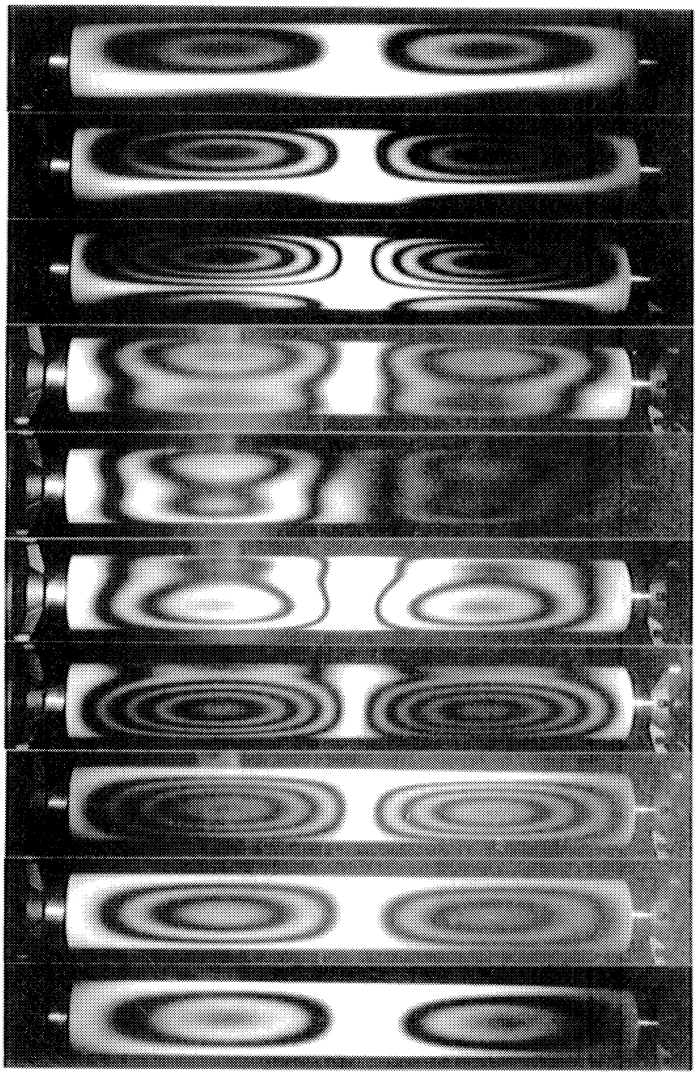

Fig. 10. Composite interferogram for uniform shell; m, n = 2, 2 mode

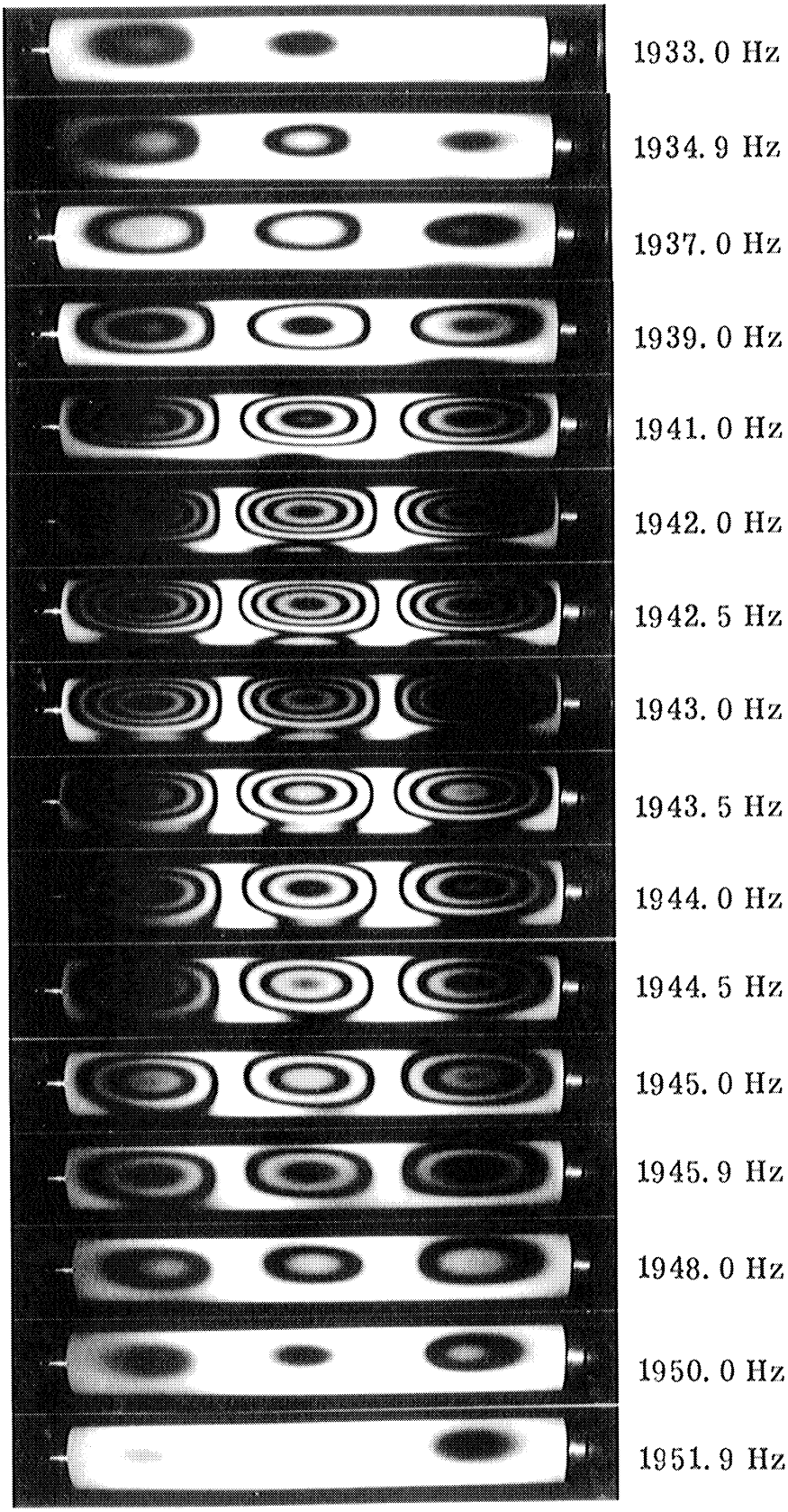

Fig. 11. Composite interferogram for uniform shell; m, n = 3, 2 mode

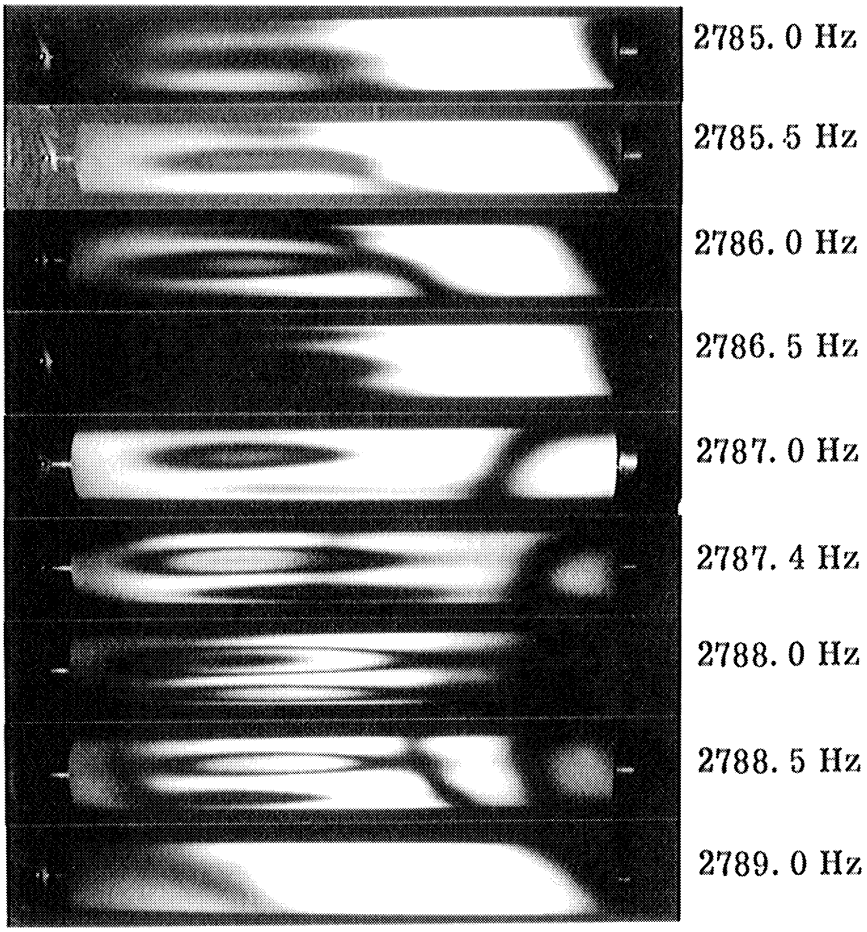

Fig. 12. Composite interferogram for uniform shell; 2787 Hz region

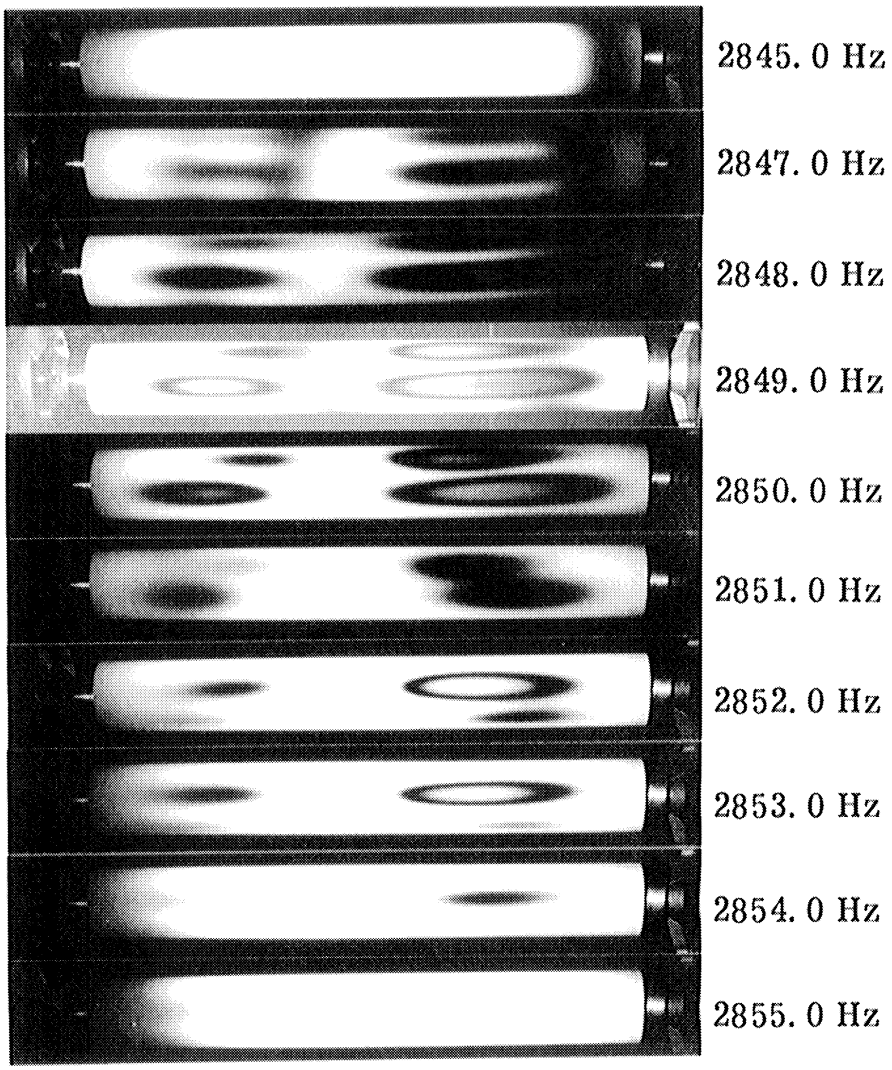

Fig. 13. Composite interferogram for uniform shell; 2850 Hz region

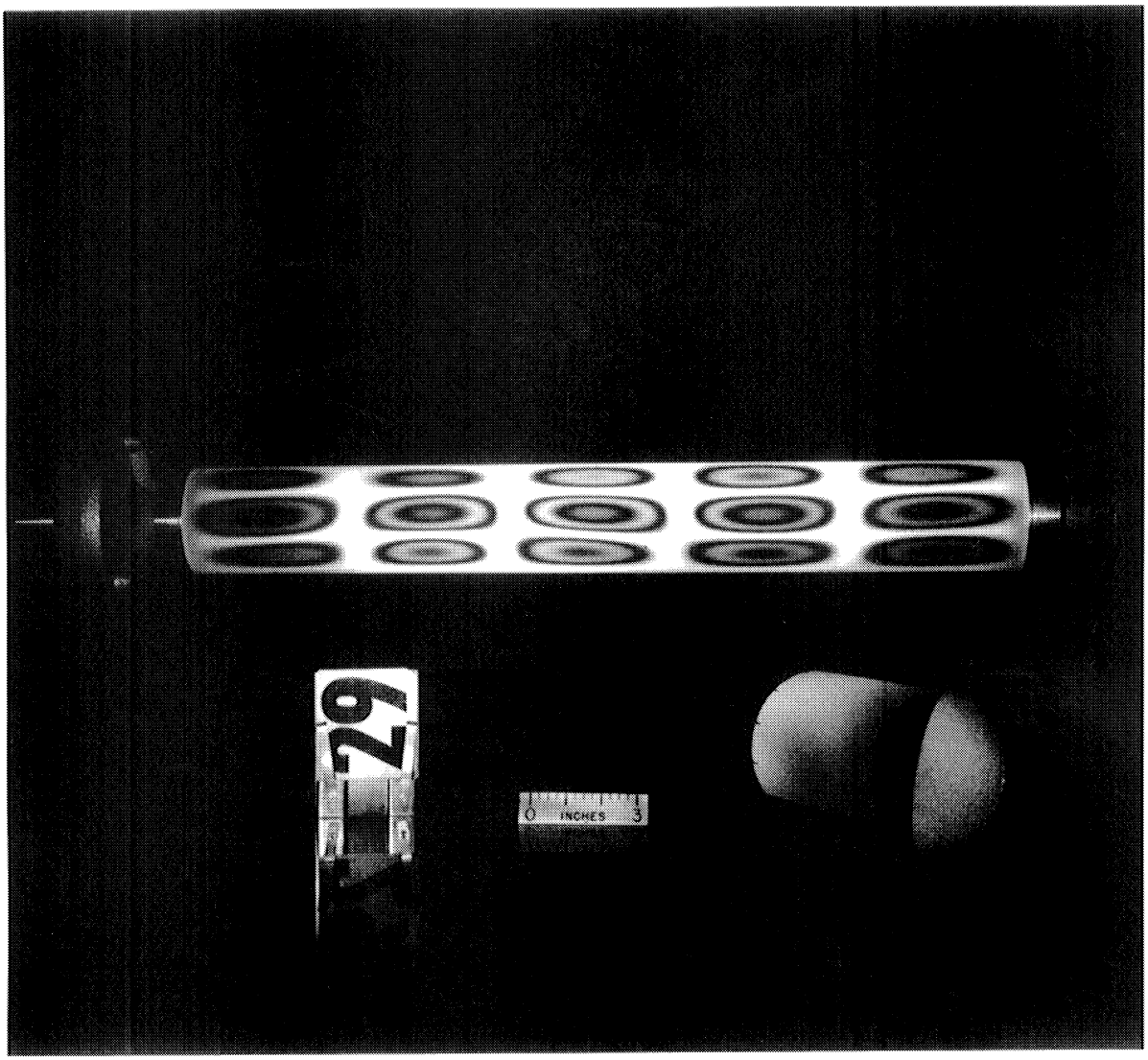

Fig. 14. Interferogram for uniform shell; m, n = 5, 4 mode

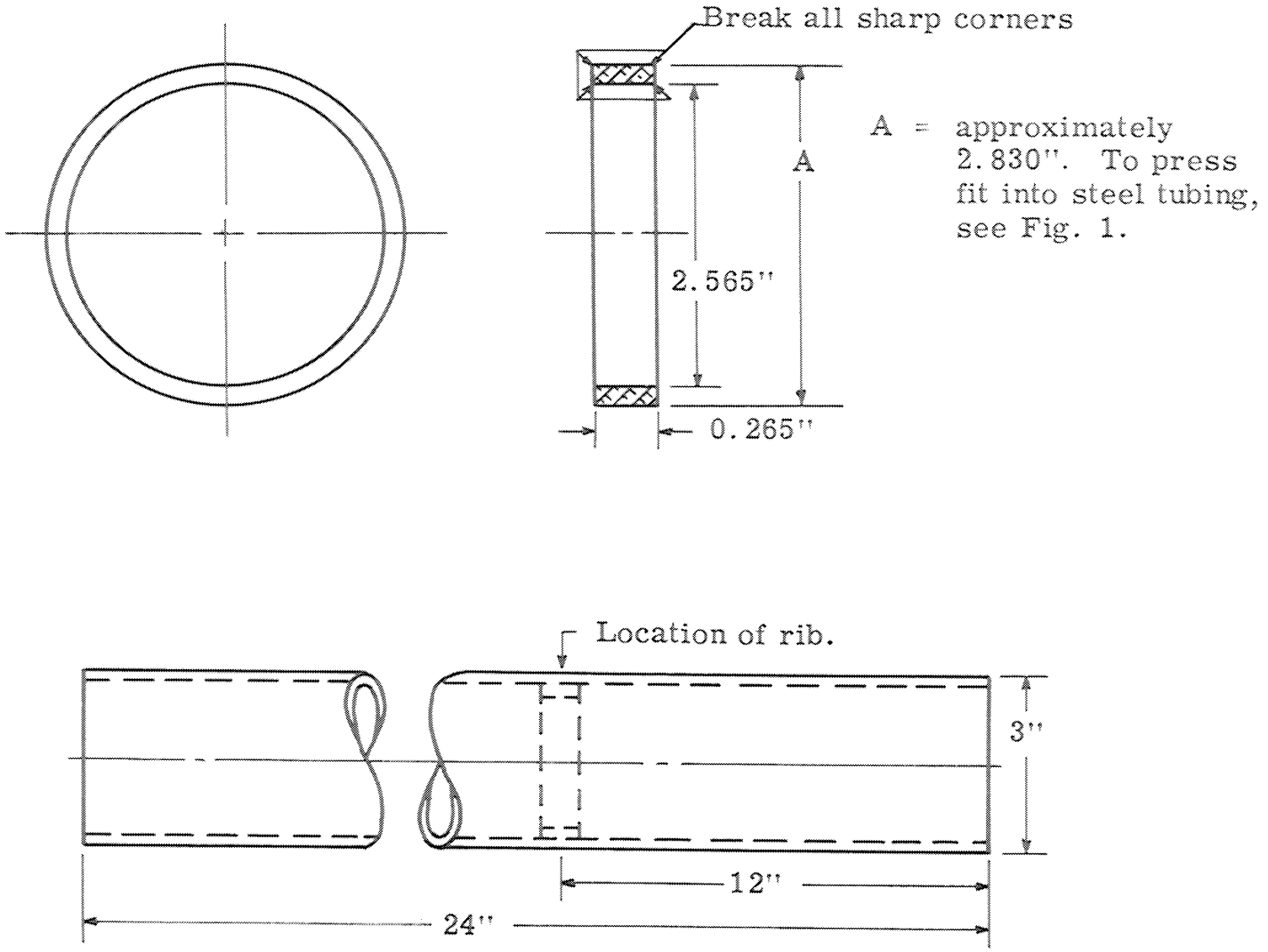

Fig. 15. Stiffening rib; dimensions and location

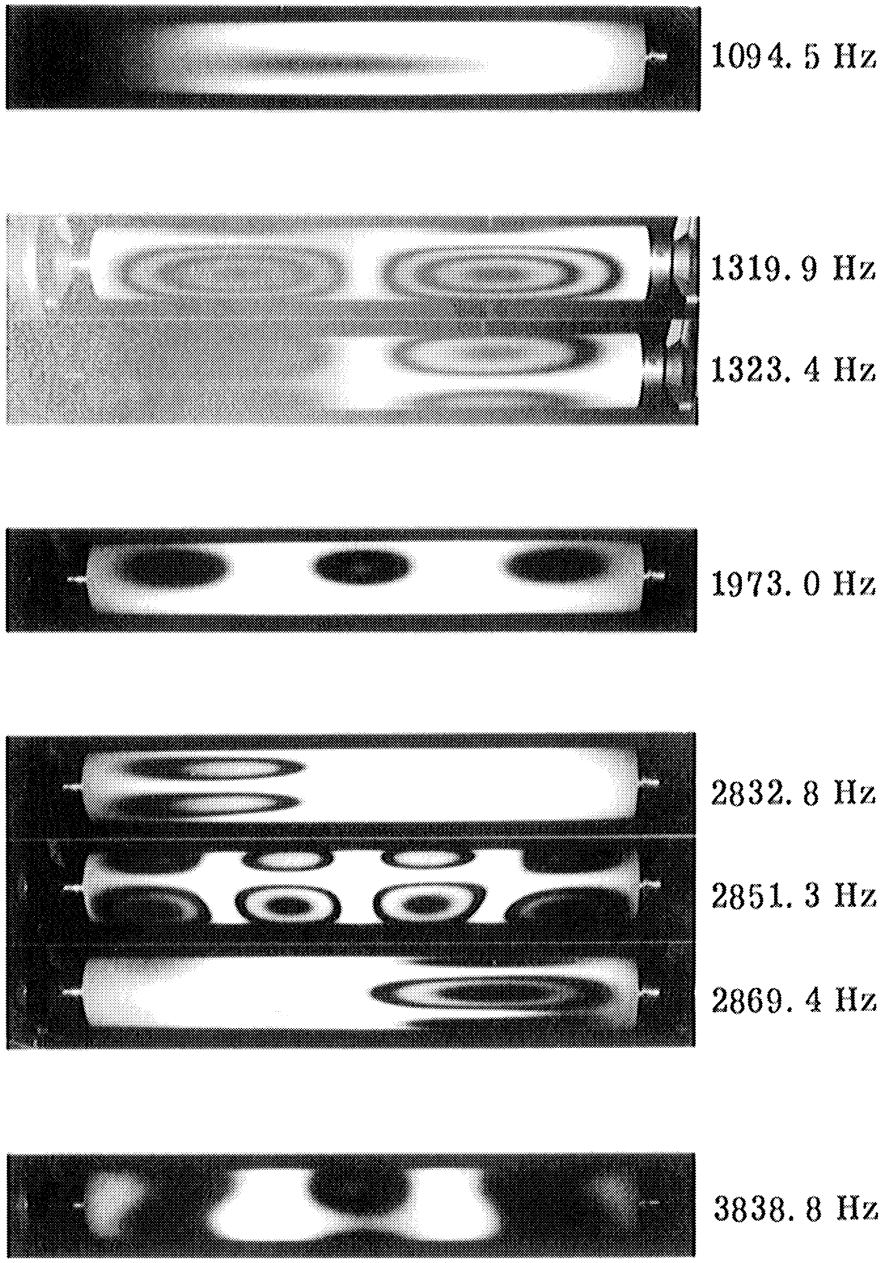

Fig. 16. Composite interferogram of mode survey of rib-stiffened shell; acoustic excitation

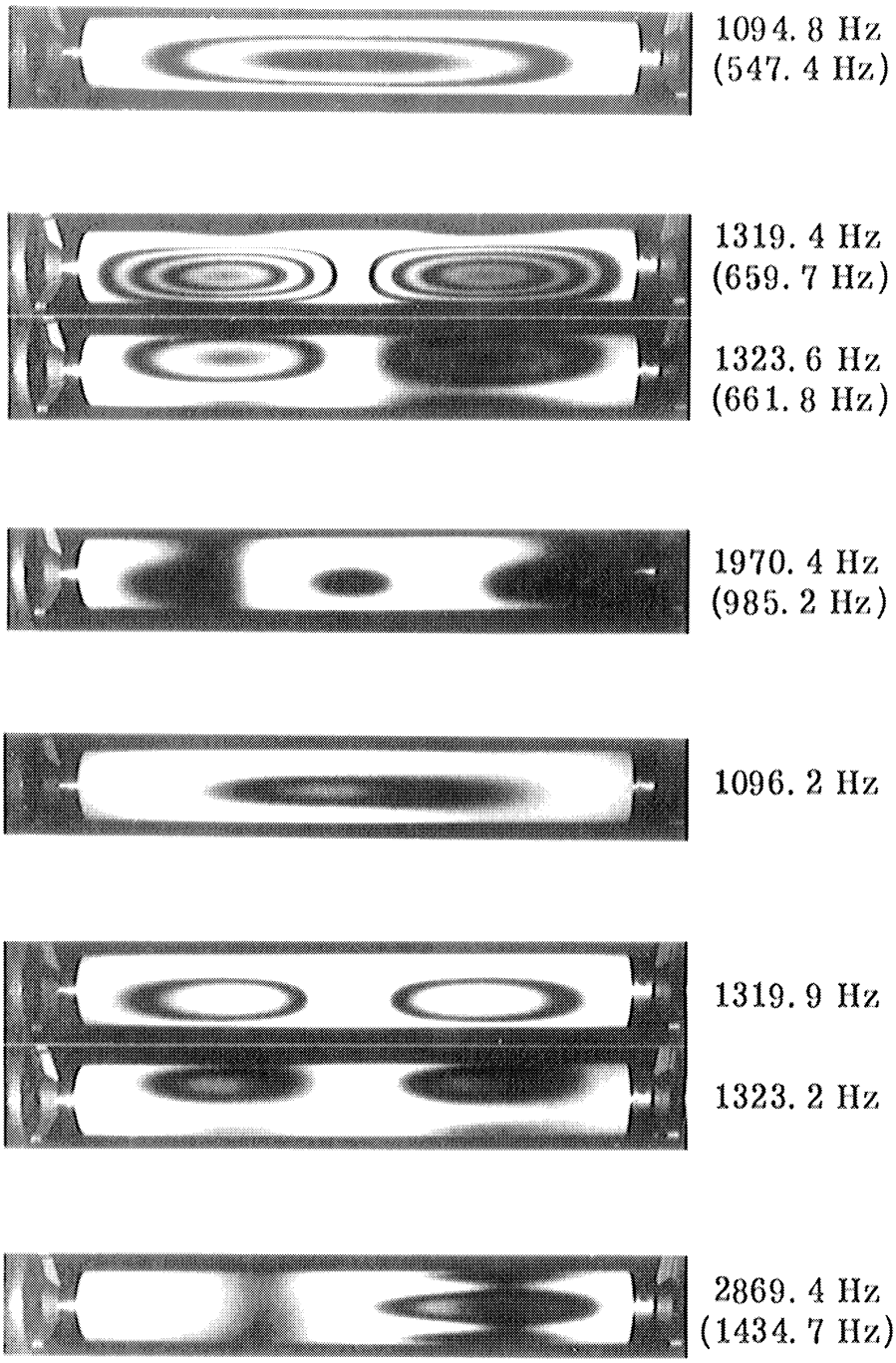

Fig. 17. Composite interferogram of mode survey of rib-stiffened shell; magnetic excitation

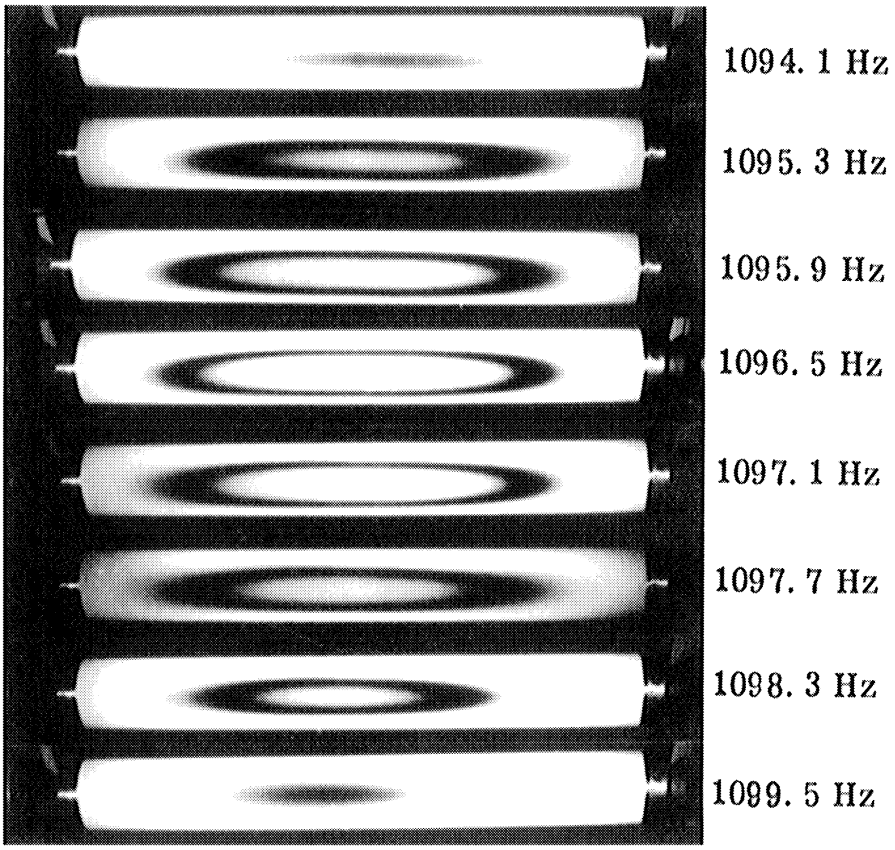

Fig. 18. Composite interferogram for rib-stiffened shell; m, n = 1, 2 mode

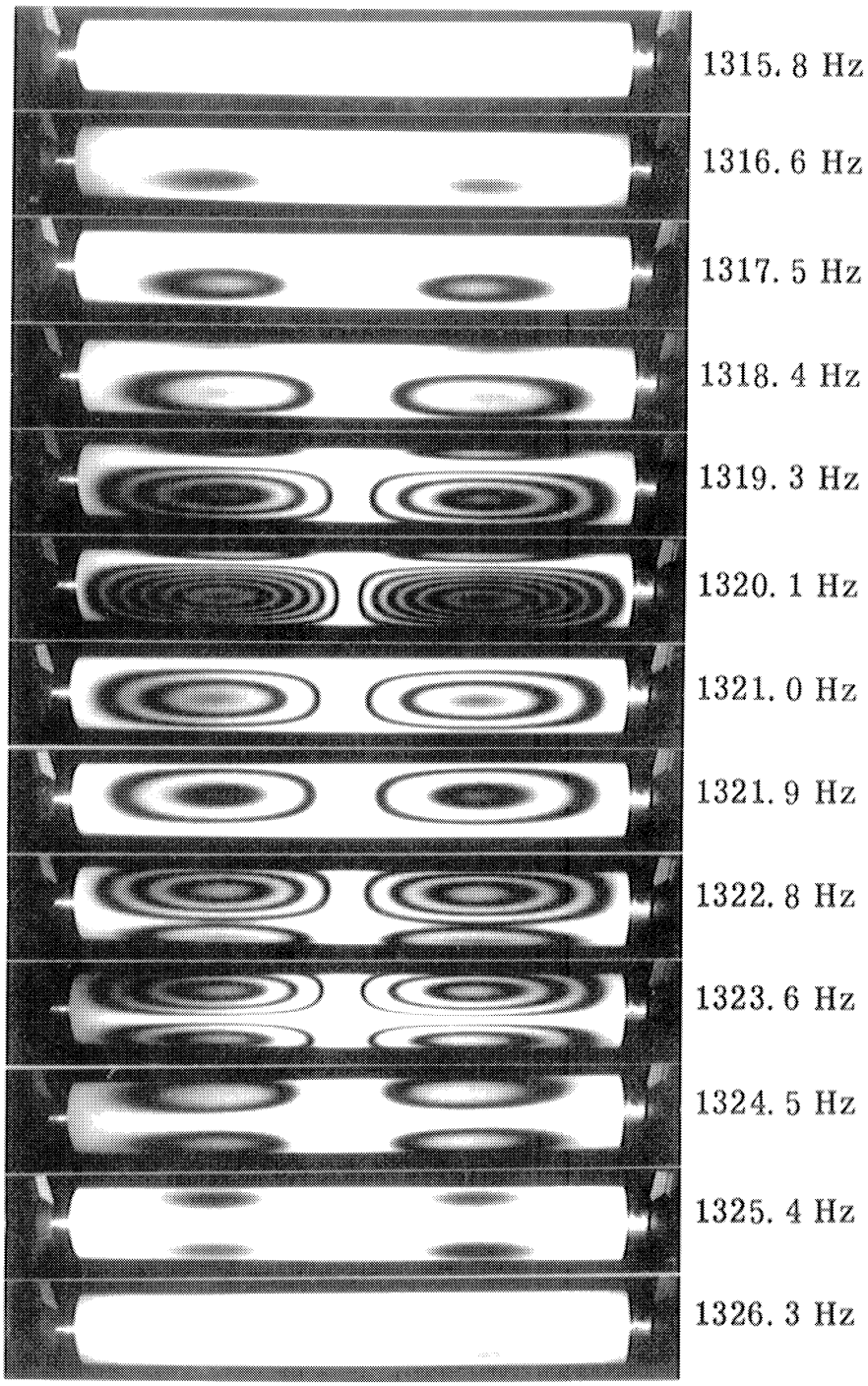

Fig. 19. Composite interferogram for rib-stiffened shell; m, n = 2, 2 mode

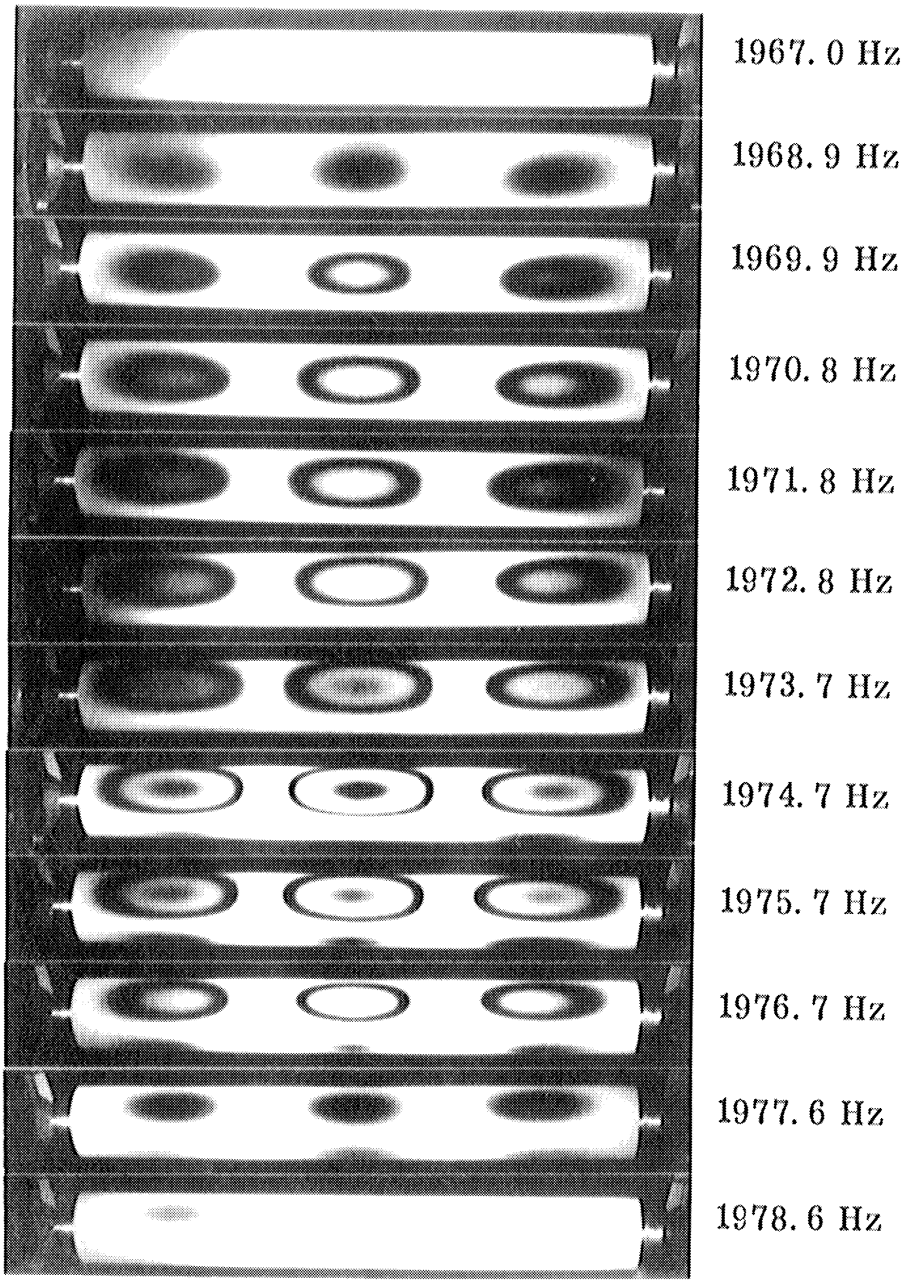

Fig. 20. Composite interferogram for rib-stiffened shell; m, n = 3, 2 mode

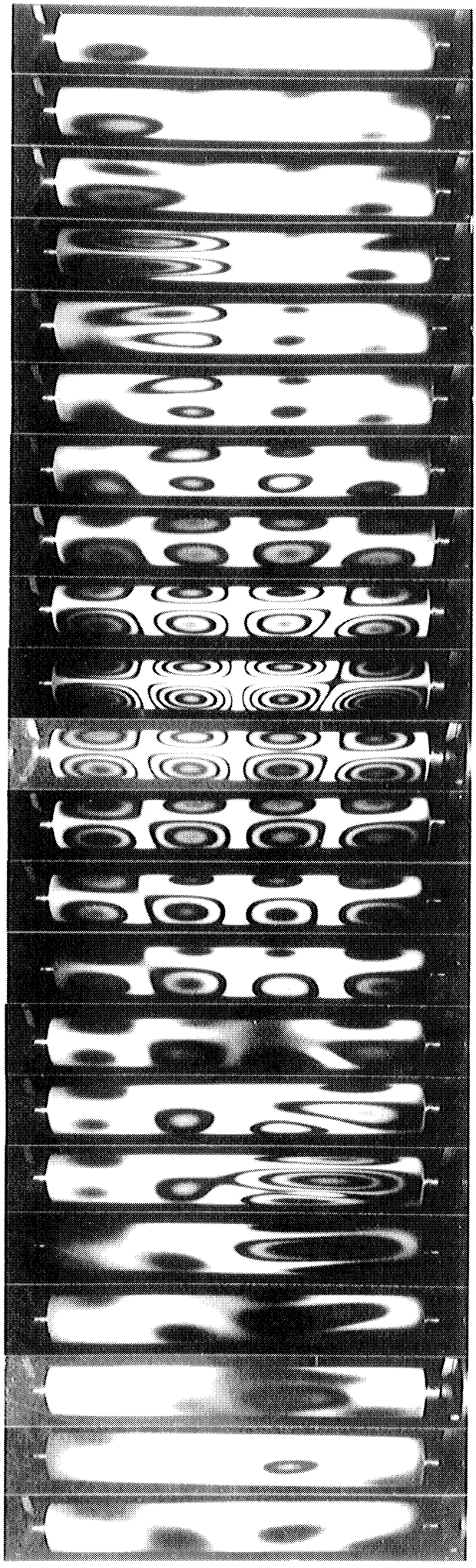

Fig. 21. Composite interferogram for rib-stiffened shell; vicinity of m, n = 4, 2 mode

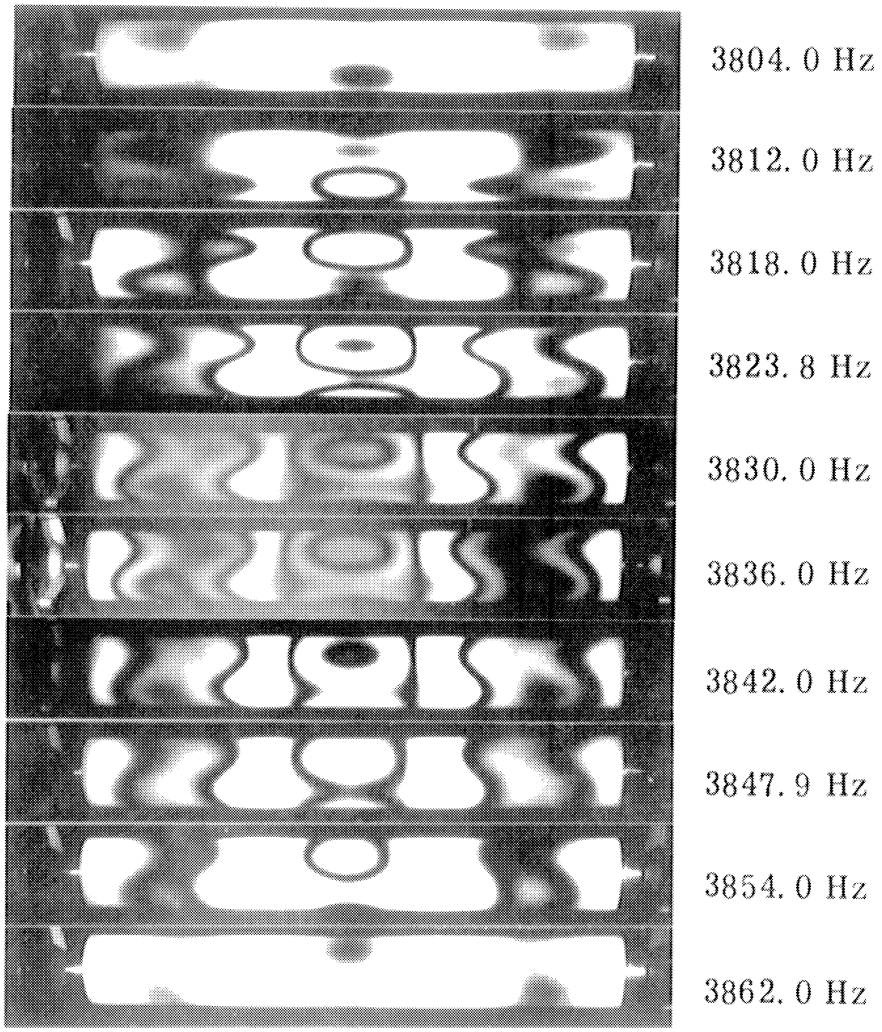

Fig. 22. Composite interferogram for rib-stiffened shell; 3835 Hz region

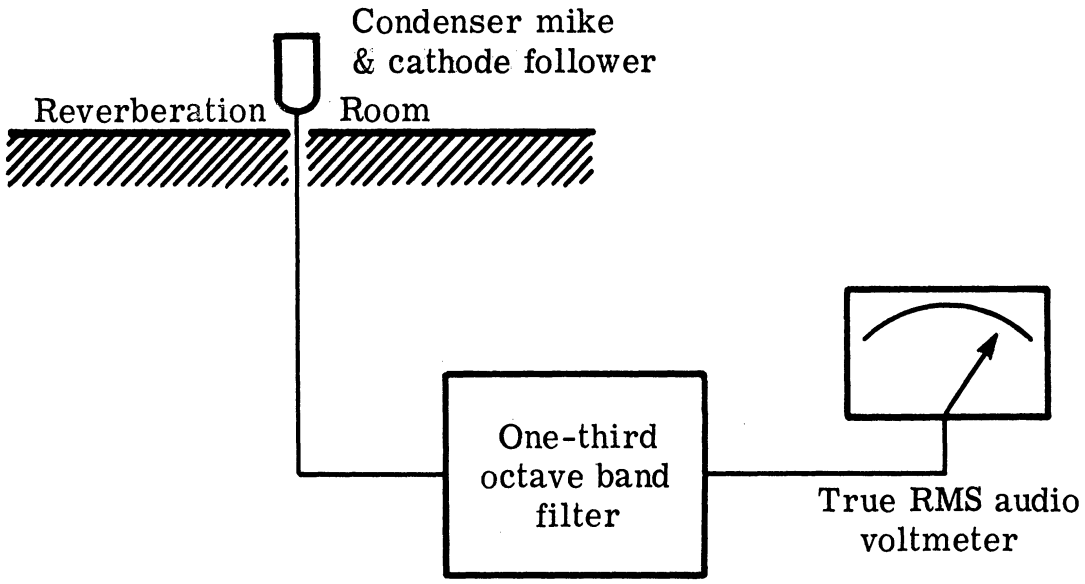

A. Sound Pressure Instrumentation

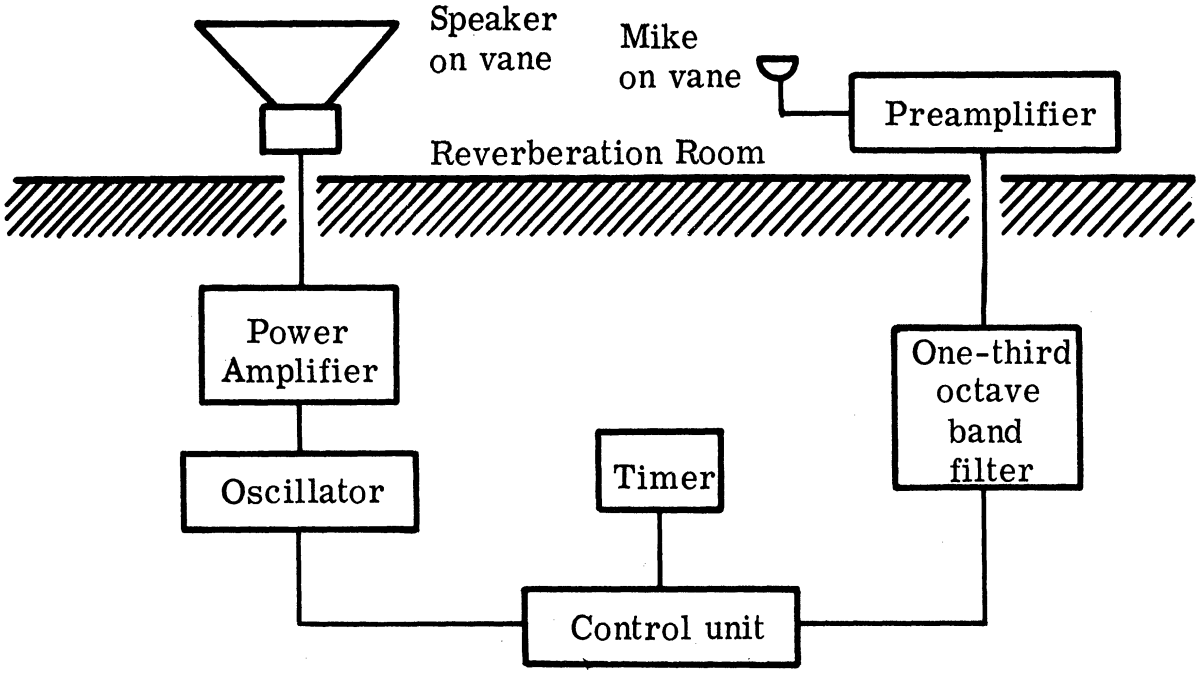

B. Decay Rate Instrumentation

For equipment details
see Appendix C. 2

Fig. 23. Block diagram of sound-power measurement instrumentation

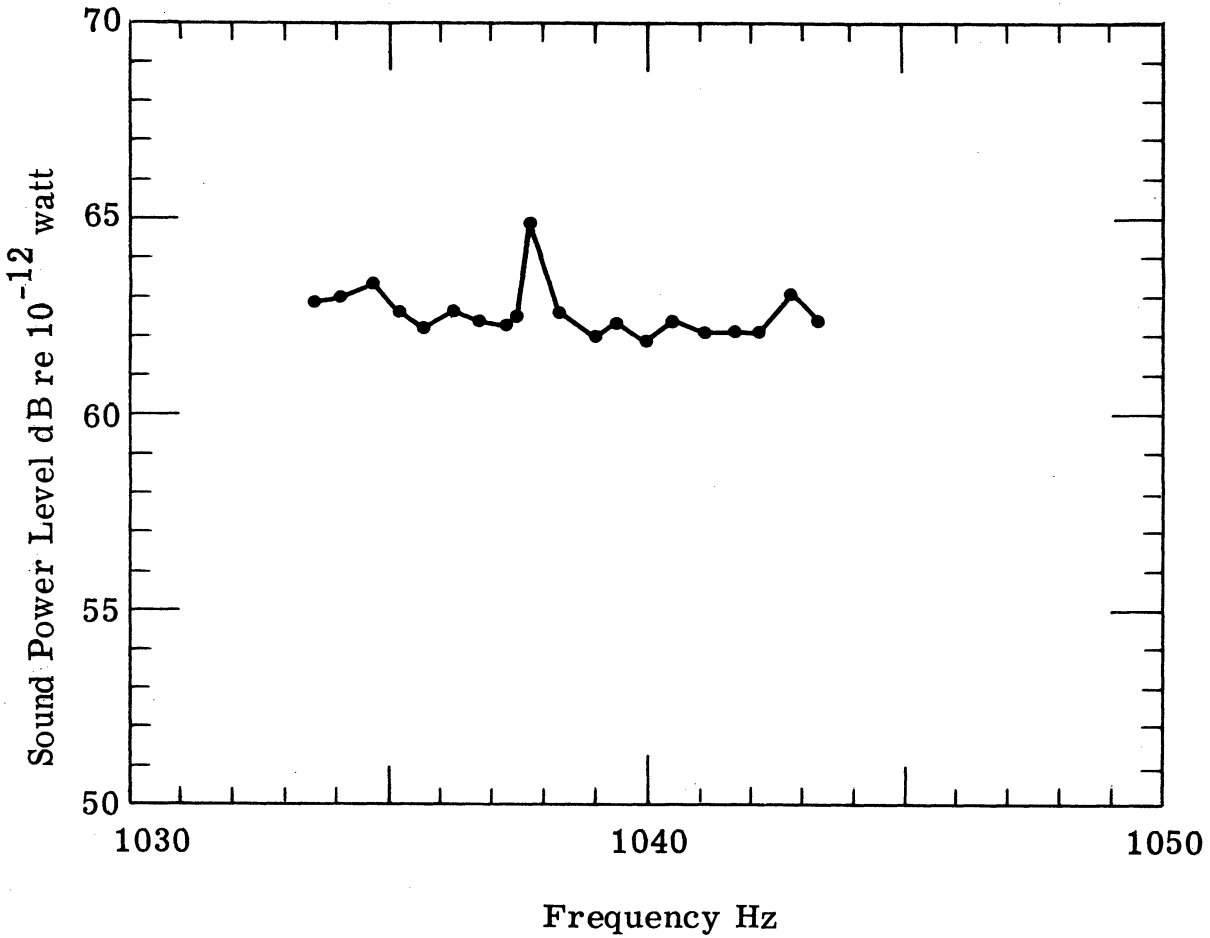

Fig. 24. Sound-power data for uniform shell; m, n = 1, 2 mode

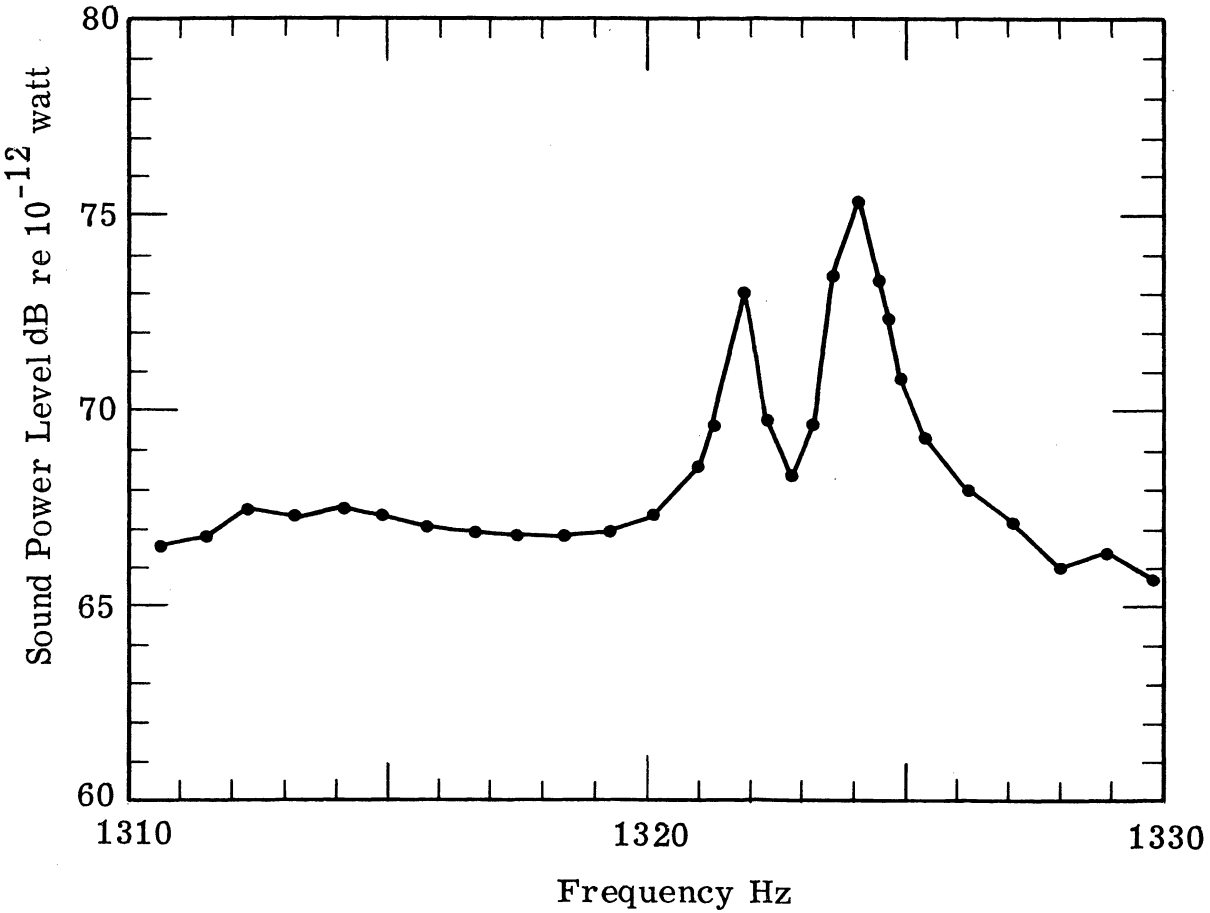

Fig. 25. Sound-power data for uniform shell; m, n = 2, 2 mode

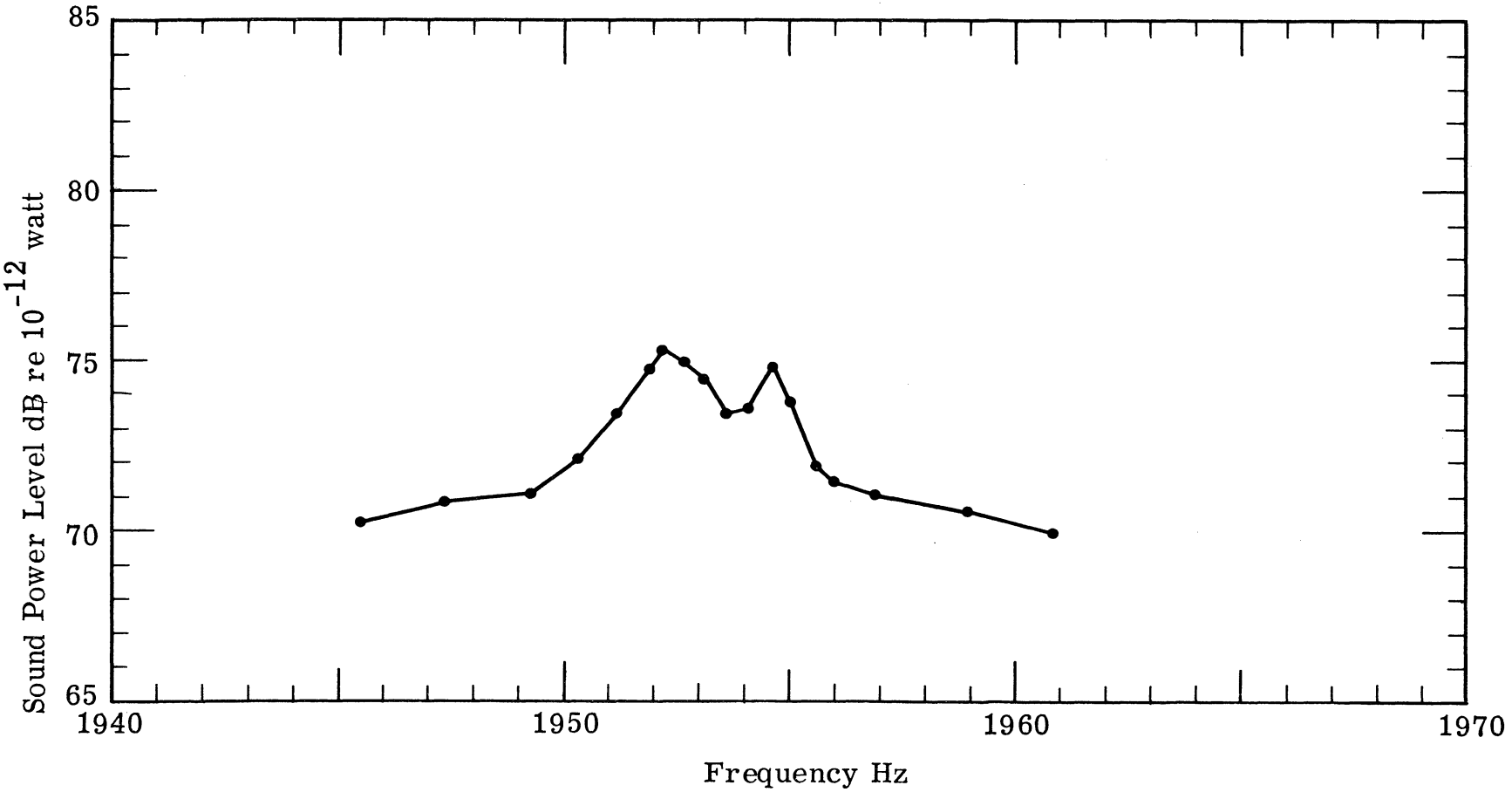

Fig. 26. Sound-power data for uniform shell; m, n = 3, 2 mode

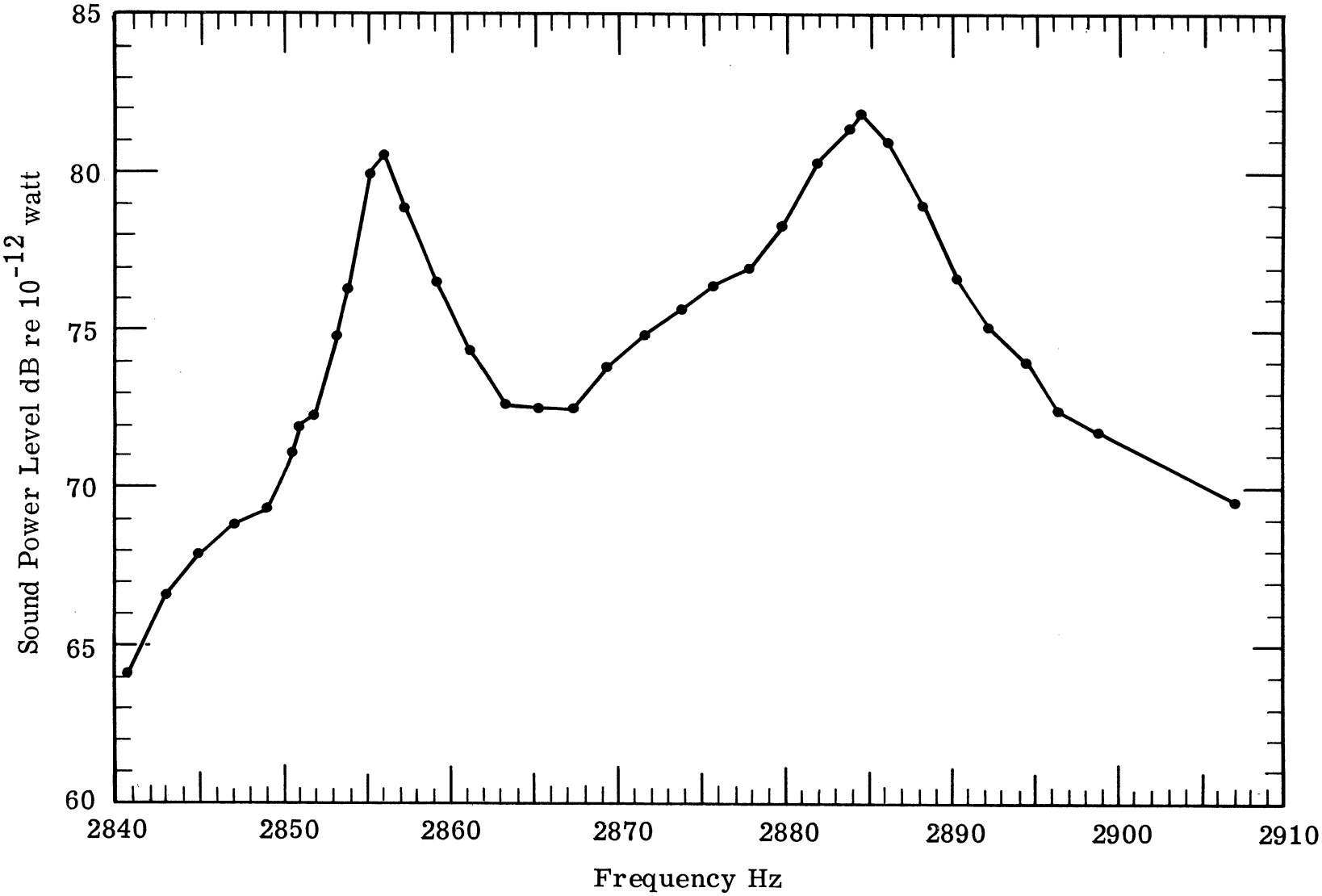

Fig. 27. Sound-power data for uniform shell; region of mode cluster

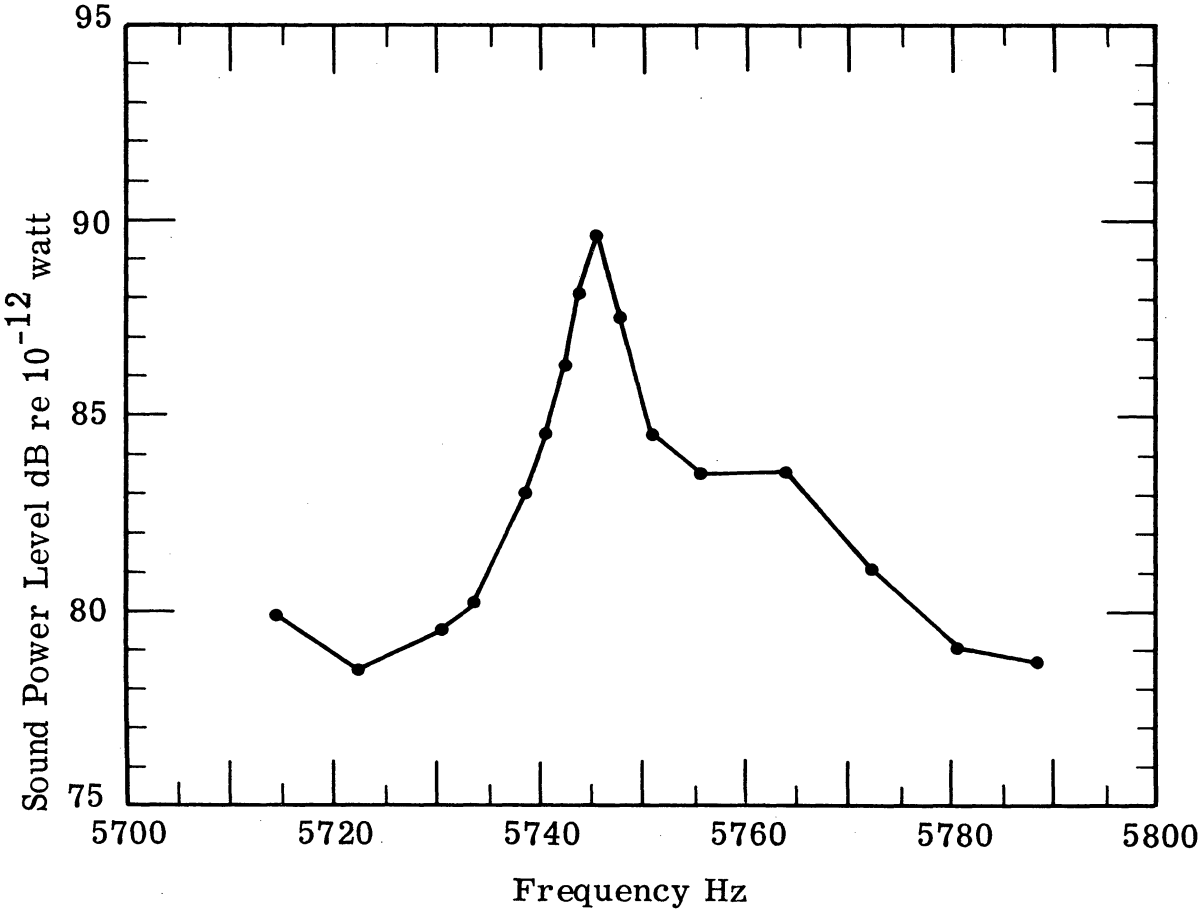

Fig. 28. Sound-power data for uniform shell; n, m = 5, 4 mode

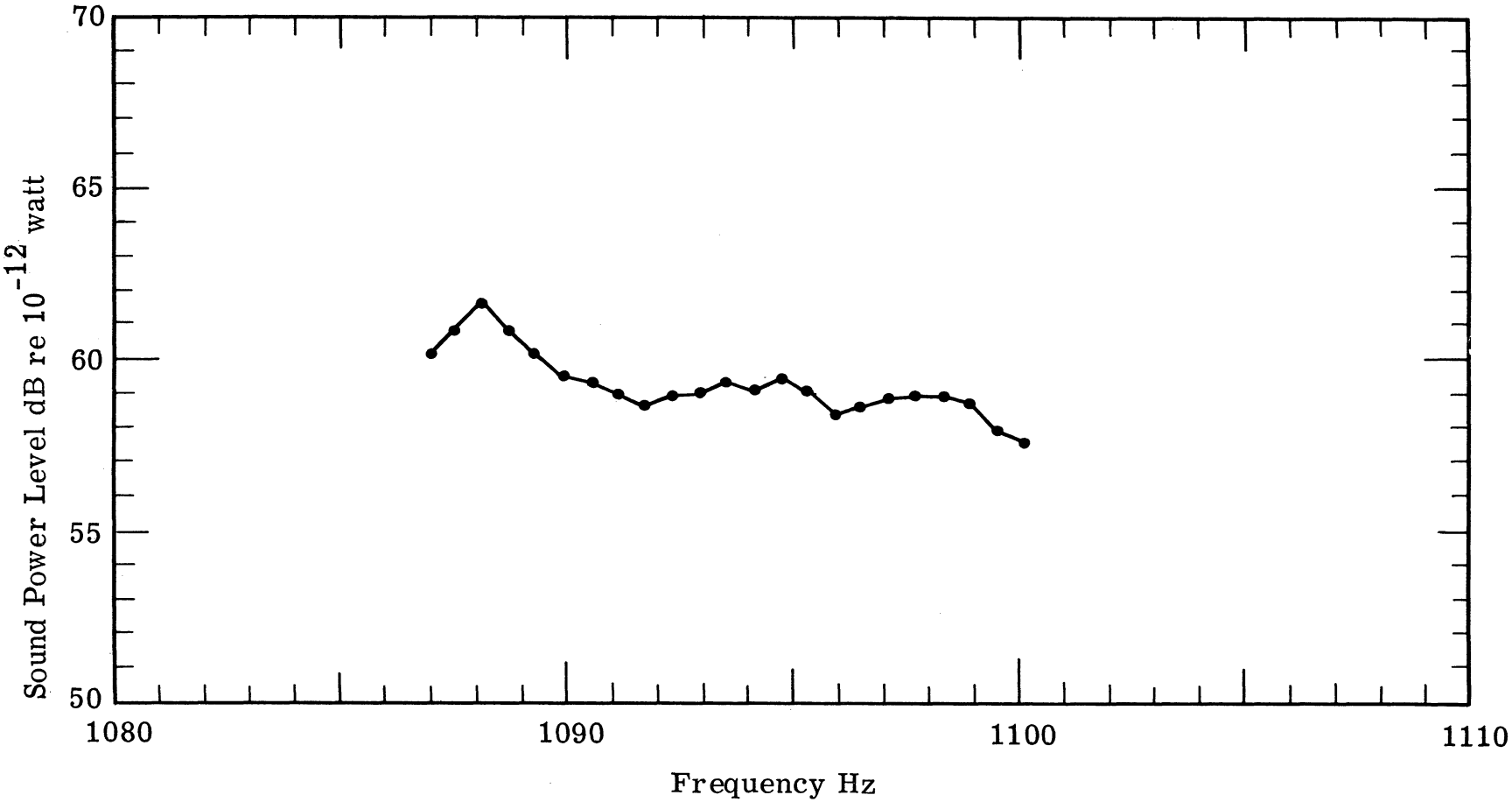

Fig. 29. Sound-power data for rib-stiffened shell; m, n = 1, 2 mode

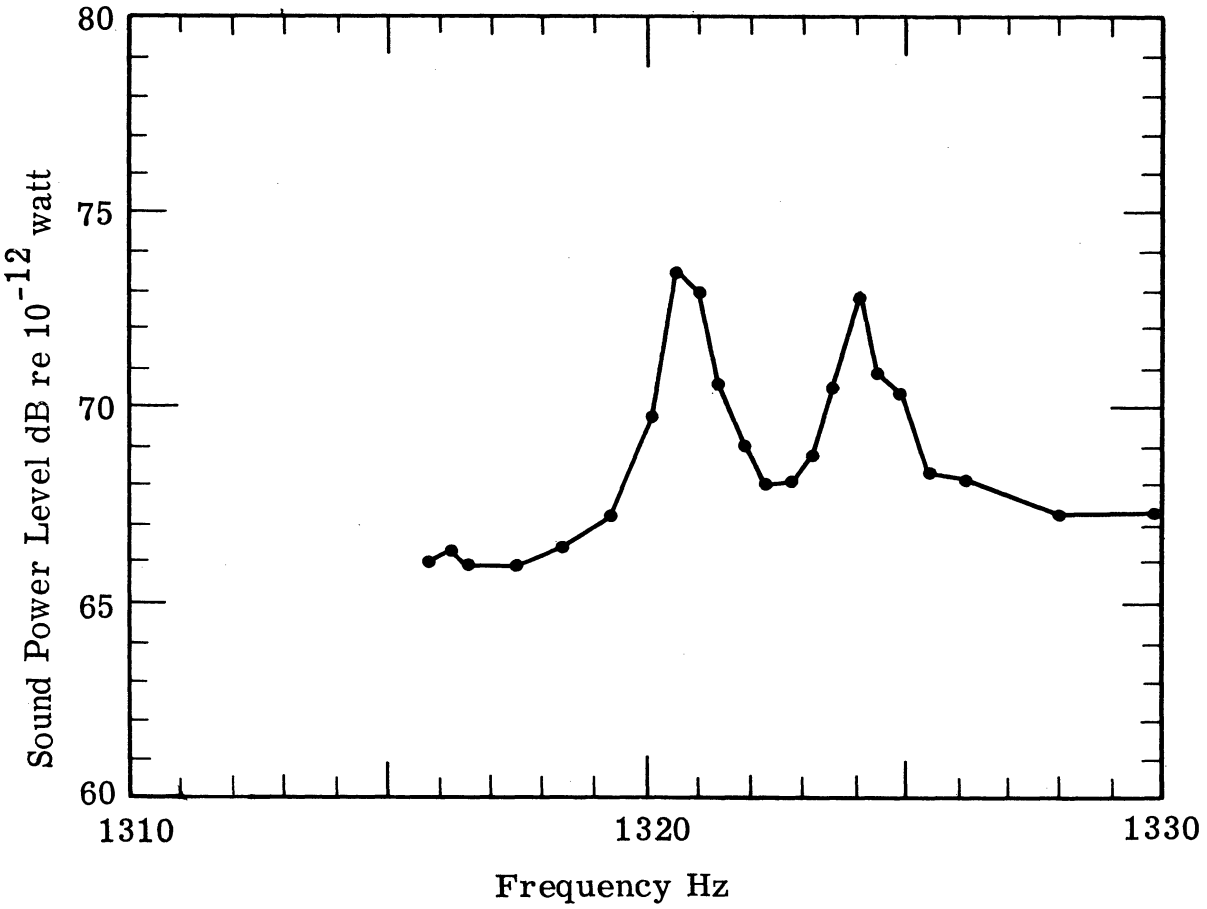

Fig. 30. Sound-power data for rib-stiffened shell; m, n = 2, 2 mode

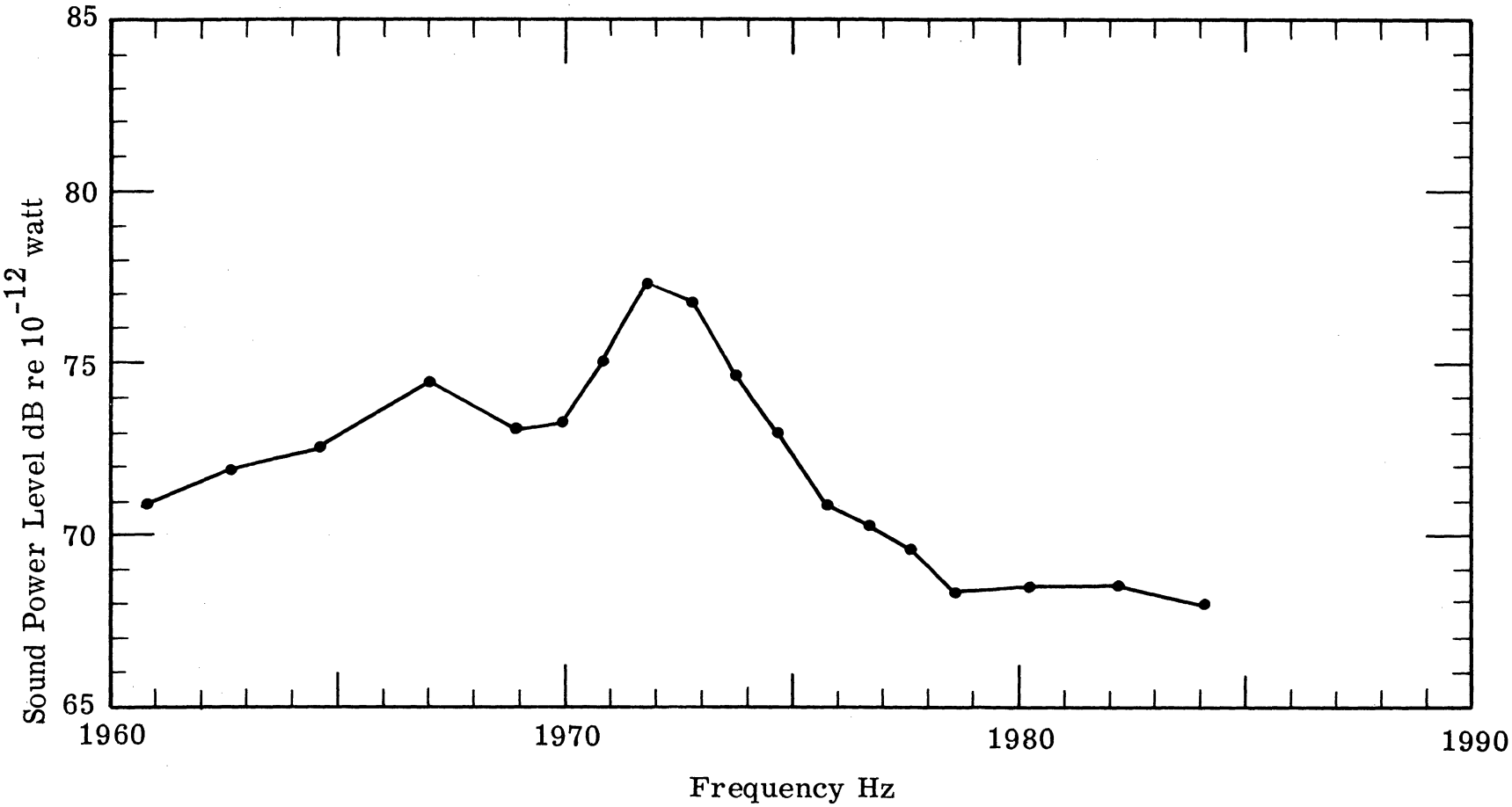

Fig. 31. Sound-power data for rib-stiffened shell; m, n = 3, 2 mode

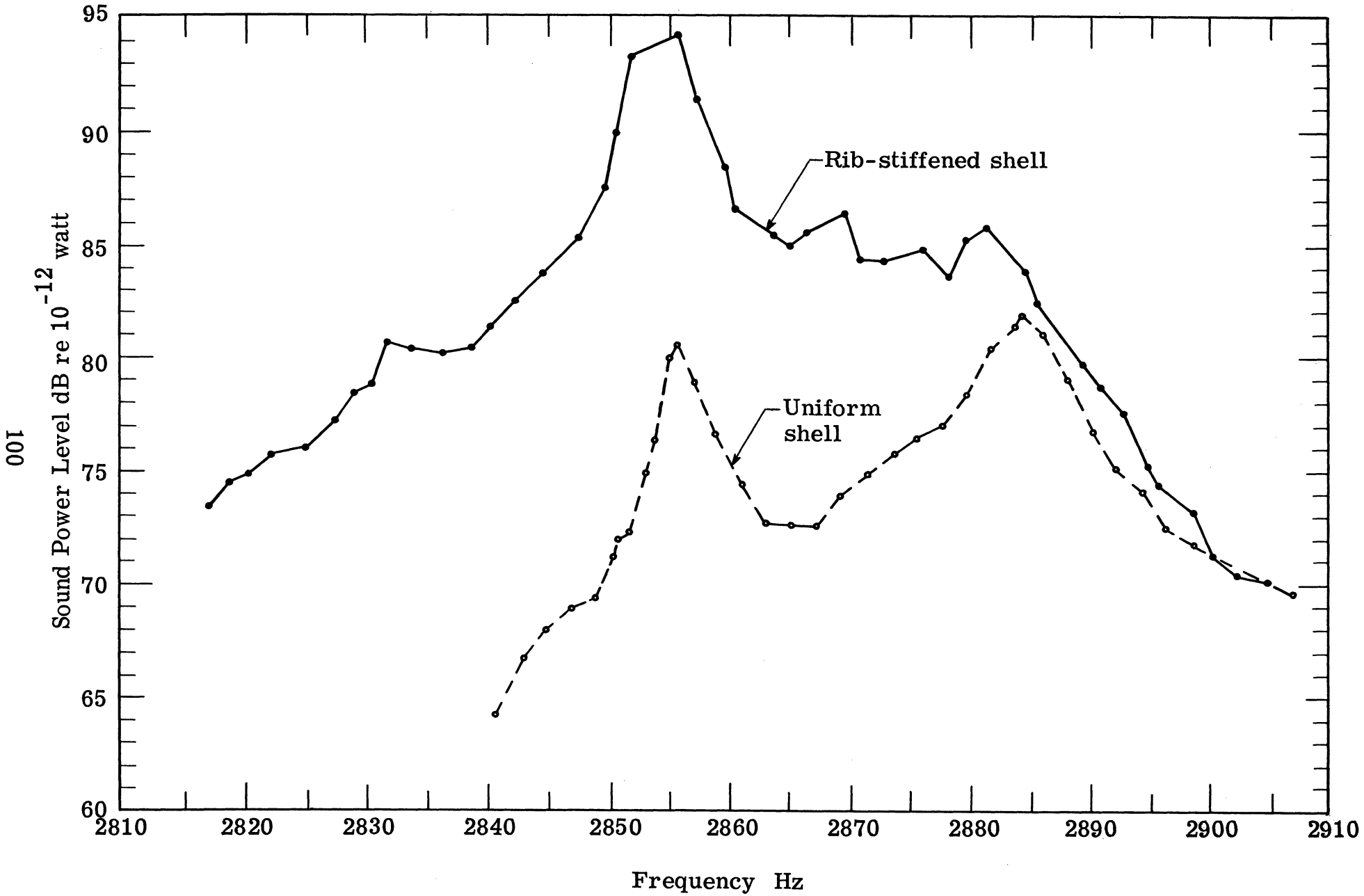

Fig. 32. Sound-power data for rib-stiffened shell; region of mode cluster; data for uniform shell superimposed

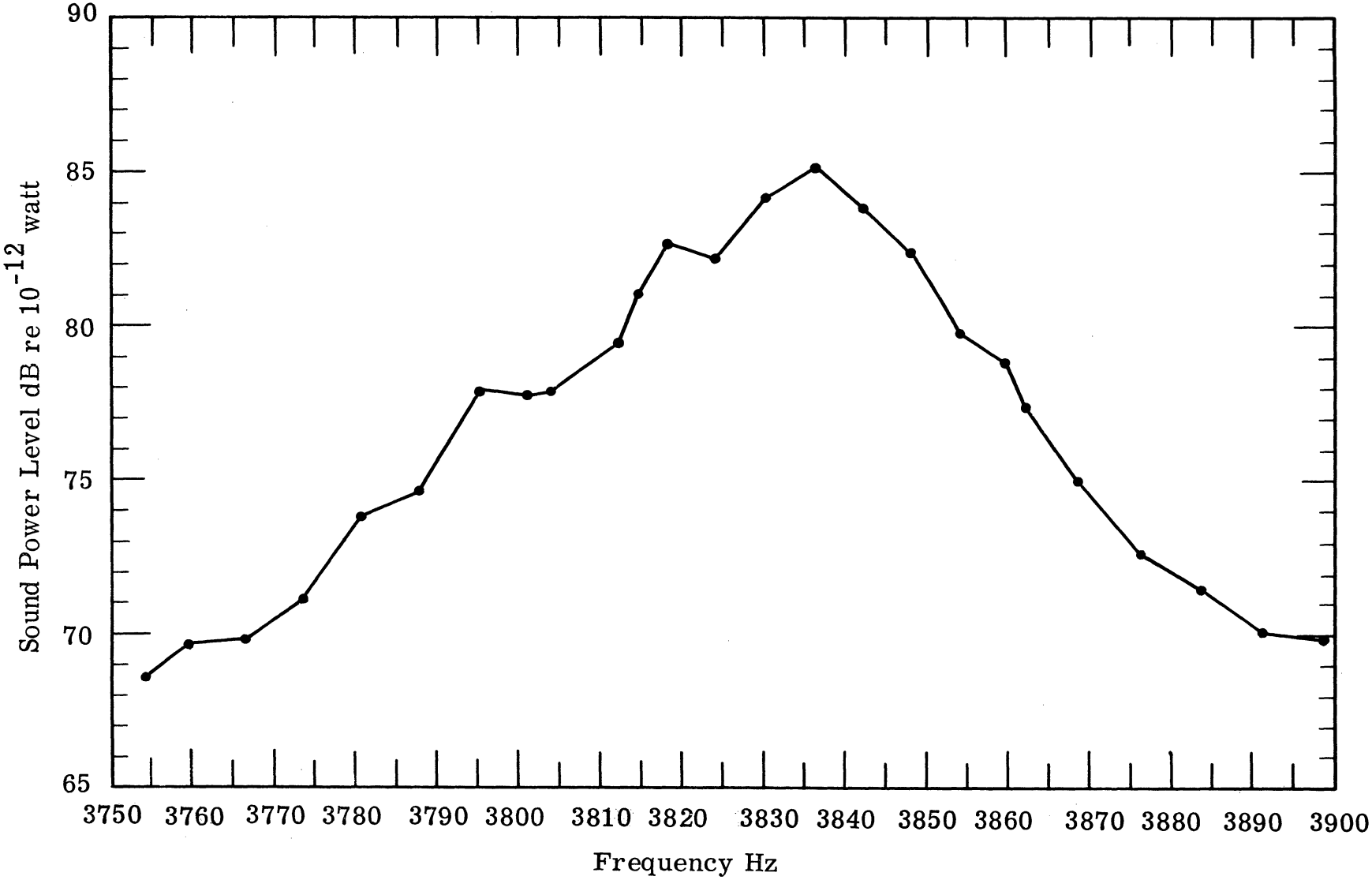

Fig. 33. Sound-power data for rib-stiffened shell; 3835 Hz region

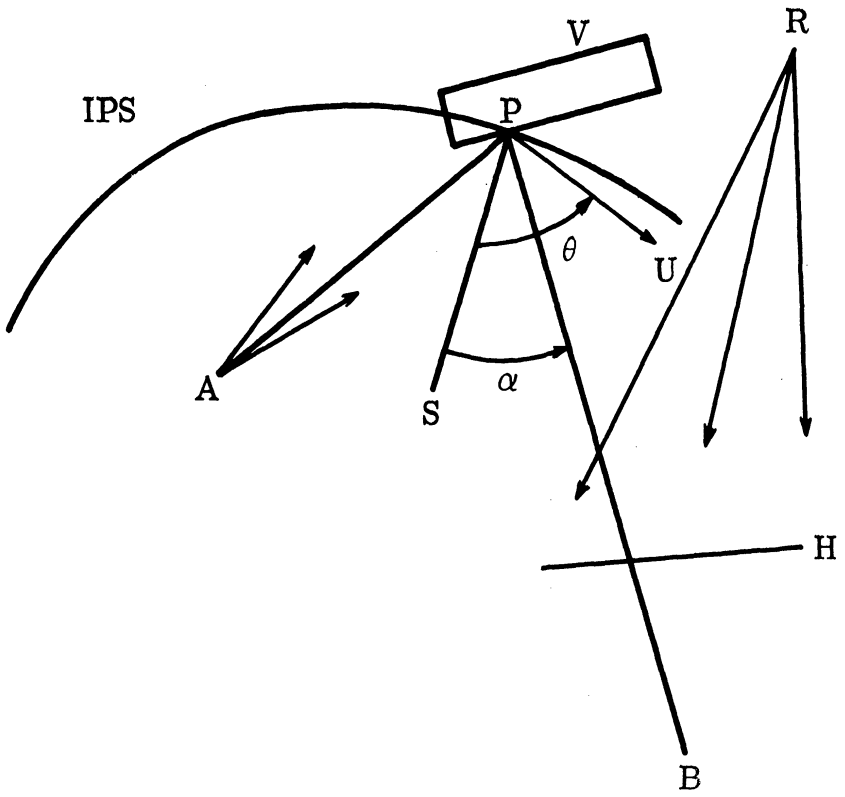

Fig. 34. Two-beam holographic arrangement for recording vibrating subject V. Subject beam source point A, viewing point B behind hologram plate H, reference beam source point R, isophase surface IPS, sensitivity vector PS, and motion vector PU for the point P.

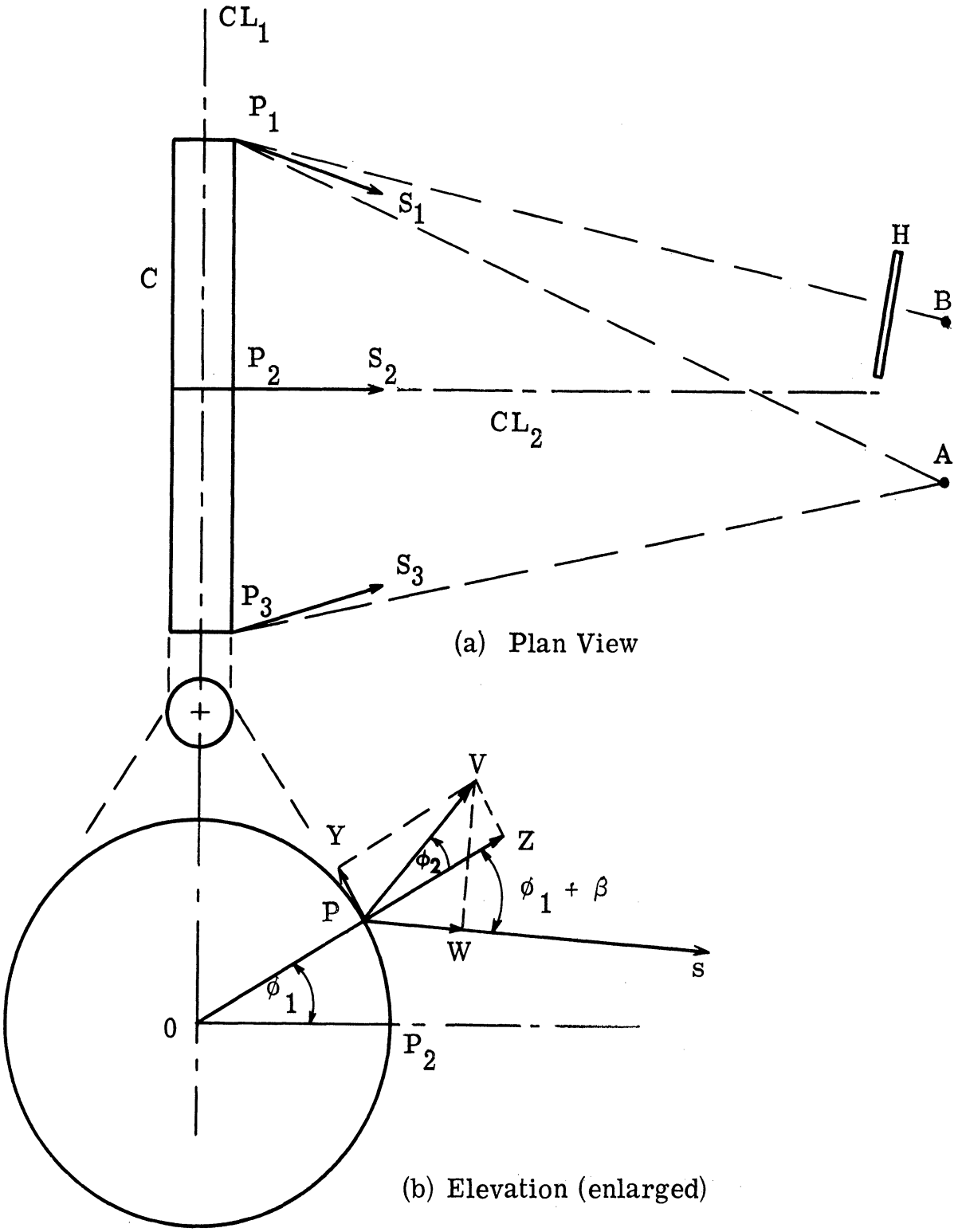

Fig. 35. Arrangement for interferograms of the 24-inch cylinder

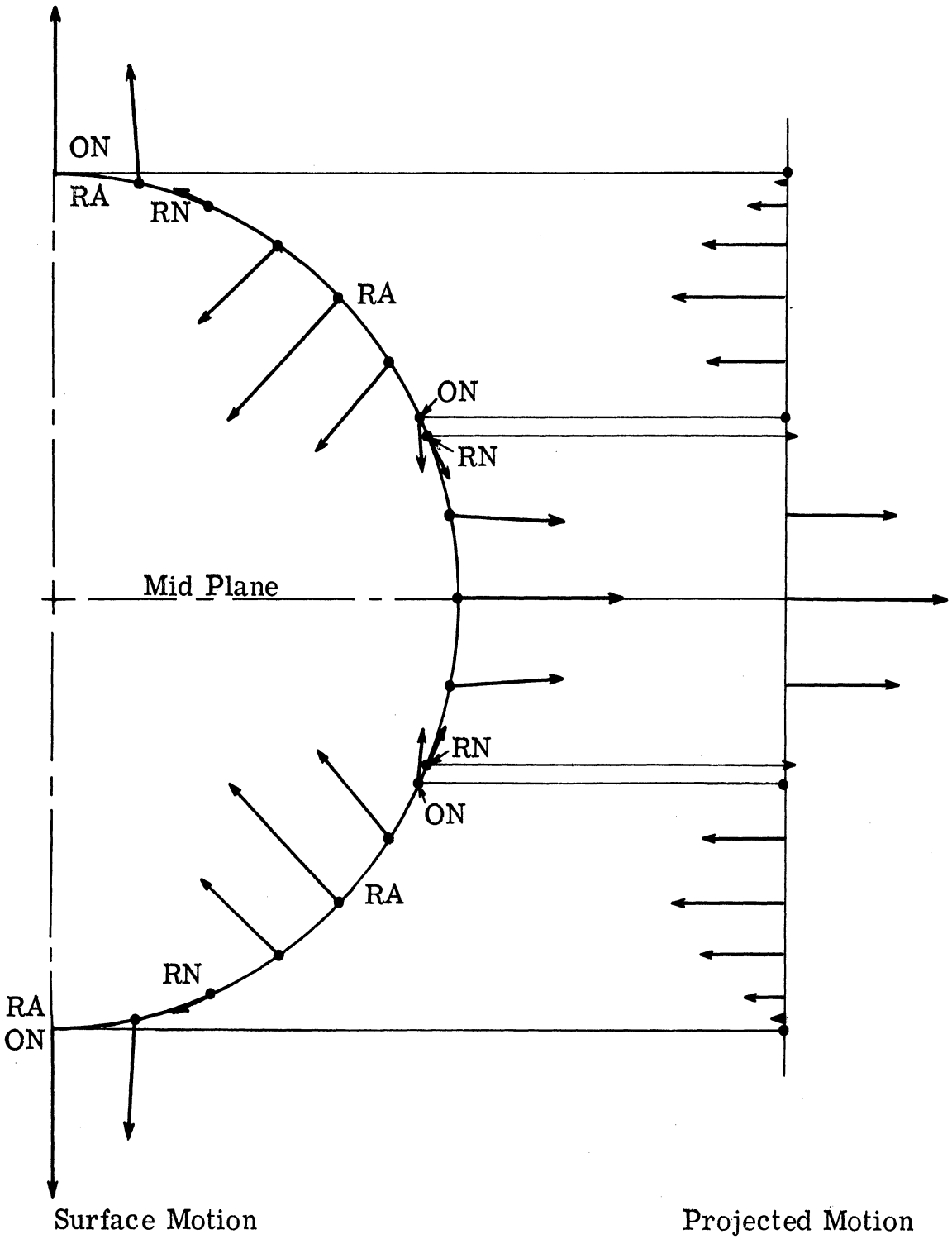

Fig. 36. Vibrational distribution in the cylinder for n = 4

APPENDIX A

REAL-TIME INTERFEROMETRY

Real-time fringes are achieved as follows. An exposed and processed hologram is returned to its holder, illuminated by the original reference laser beam, and adjusted such that its virtual image is in almost exact register with the subject. The latter is also illuminated with its original beam just as during the exposure. If done properly, this results in real-time interference between the subject and its virtual image, giving fixed, parallel fringes of almost any desired spacing.

The fringes are seen by viewing the subject and image directly from behind the hologram plate. For real-time interferometry, our practice is to expose for a plate density somewhat above normal in order to improve the visibility of fringes. The fringe contrast ratio is optimized at a plate density of about 1. 1.

Real-time interferometry is important both as a qualifying method for examining the stability of the holographic apparatus, and as a survey tool in vibration analysis. The fringes are motionless if the subject and all other optical parts have sufficient stability. Drifting fringes indicate motion, such as might be due to thermal relaxation. Shaking fringes indicate low-frequency vibration which must be eliminated before any further holograms may be made.

Equally important is the use of real-time fringes for vibration survey work. If the subject is driven externally at a slowly varying frequency, the fringes wash out in areas where resonant responses are obtained. The preliminary vibration survey may thus be done directly, with resonant frequencies and appropriate driving levels being noted for future time-average interferograms.

APPENDIX B

PRACTICAL HOLOGRAPHY

The following items dealing with laboratory practice in holography are noted below for record purposes.

B. 1 Laser Coherence Length

The coherence length of the Spectra Physics Model 125 helium-neon laser is ±20 cm (8 inches). This is typical of all conventional helium-neon lasers not equipped with coherence stretchers. As a consequence, for adequate image brightness in holography, the cumulative light path length (as measured from the beam splitter to the center of the hologram plate) of the subject beam must not differ from that of the reference beam by more than about 10 cm, so that one is well within the coherence length. This restricts the depth of the subject which may be holographed with the conventional 2-beam arrangement. For situations requiring longer path length differences, the laser must be equipped with a coherence stretcher, such as an intercavity etalon.

B. 2 Beam Ratio

Laboratory practice shows that the ratio of intensities (I_r / I_s) of the reference to subject beams as measured at the plate holder should be at least 3 for perserving linearity, and no greater than about 15 for a

usable image brightness of the reconstructed image. Routinely, a ratio of between 4 and 6 was used.

B. 3 Plate Density

The brightness of the reconstructed image depends upon the density of the hologram. The reconstruction efficiency of this image reaches a broad maximum for an average hologram plate density * of 0. 6. Our practice has been to hold the plate density within 0. 1 unit of optimum, except for special purposes (Appendix A). The efficiency falls to 70 percent of its maximum value for plate densities of 0. 3 and 1. 0. These results were obtained in an evaluation survey of Agfa-Gevaert 10E70 plates developed to a gamma of 4. 3.

B. 4 Plate Processing for Consistent Hologram Quality

For Eastman 649F and Agfa-Gevaert 10E70 plates, the following precessing routine was followed. Processing trays were held at a constant temperature of 68° F by partial submersion in a large bath of temperature-controlled running water at 68° F. Plates were processed emulsion side up with continuous agitation in total darkness through step (c) below.

(a) Develop in fresh Kodak D-19 4. 5 min at 68° F (5. 0 min for Agfa 10E70).

(b) Short stop in Kodak SB-5 for 0. 5 min.

*Semidiffuse density.

(c) Fix in Kodak Rapid Fixing Bath for 4. 0 min.

(d) Rinse in running water for 0. 5 min.

(e) Kodak Hypo Clearing Agent for 2. 0 min.

(f) Wash in running water for 5. 0 min.

(g) Dip in Kodak Photoflo Solution for 10 sec.

(h) Drip-dry plates in vertical position in still air at room temperature.

This processing gives a gamma of approximately 4. 0 for 649F and approximately 4. 3 for 10E70 emulsion.

B. 5 Evaluation of Agfa-Gevaert 10E70 for Helium-Neon Holography

This emulsion represents an advance in speed and efficiency for holography. The speed is 37 times that of Eastman 649F. The quality of the hologram image is equally as good as 649F, and there appears to be greater efficiency in image reconstruction. The Agfa emulsion is, however, somewhat noisier than 649F, producing more diffusely scattered light, and therefore reducing the visibility of shadow detail in the hologram image.

B. 6 Exposure Control

Since hologram plates were developed to a gamma of roughly 4. 0, increasing the exposure by 6 percent caused an increase in plate density of 0. 1 unit. Since it was found desirable to hold the plate within 0. 1 unit of the desired density, precise exposure control was therefore

required. To be within 6 percent of the target value on exposure, the combined errors in both intensity and exposure time had to be less than 6 percent.

For this reason the intensities of both the subject beam and reference beam were measured just prior to exposure. Furthermore, the reference beam intensity was made as uniform as possible over the plate area. Timing was controlled with a contacting clock with resetable sweep second hand operating a solenoid-actuated shutter in the path of the laser beam. This method gave satisfactory timing control for exposures longer than 2 or 3 seconds.

APPENDIX C

TABULATED DATA

C. 1 Components of Drive Instrumentation (Refer to Fig. 3.)

Acoustics drivers:	Electro-Voice (Electro-Voice, Inc., Buchanan, Michigan Type 1829
Magnetic exciter:	Laboratory built
Power amplifier No. 1:	McIntosh (McIntosh Laboratory, Inc., Binghamton, New York) Type MC-250
Power amplifier No. 2:	Laboratory built
Step attenuator:	Daven (The Daven Co., Newark, New Jersey) Type VT-790G
Oscillator:	Waveforms (Waveforms, Inc., New York, New York) Model 401E
Frequency counter:	H. P. (Hewlett-Packard Co., Palo Alto, California) Model 5245L
Audio-frequency voltmeter:	H. P. Model 3400A
Oscilloscope:	Tektronix (Tektronix, Inc., Beaverton, Oregon) Type 516

C. 2 Components of Sound-Power Instrumentation (Refer to Fig. 23)

A. Sound Pressure Instrumentation

Microphone:	Bruel and Kjaer (B & K Instruments, Inc., Cleveland, Ohio) Type 4134 1/2" diam condenser microphone Type 2615 cathode follower
Spectrometer:	Bruel & Kjaer Type 2142 audio frequency spectrometer
RMS voltmeter:	Ballantine (Ballantine Laboratories, Inc., Boonton, New Jersey) Model 320 true root-mean-square voltmeter

B. Decay-Rate Measurements

Warble oscillator:	Bruel & Kjaer Type 1014 beat frequency oscillator
Power amplifier:	McIntosh (McIntosh Laboratory, Inc., Binghamton, New York) Type MC 30
Loudspeakers:	GE (General Electric Co., Auburn, New York) Model 1201 B 12" wide range speaker
Microphone:	Bruel & Kjaer Type 4134 and 2615 (battery operated)
Preamplifier:	Tektronix (Tektronix, Inc., Portland, Oregon) Type 122 low-level preamplifier
Filter:	Bruel & Kjaer Type 2142 audio frequency spectrometer
Timer:	Beckman (Beckman Instruments, Inc., Richmond, California) Model 736 OR Universal eput and timer
Control:	Special laboratory-built circuitry

C. 3 Typical Sound-Power Data for Uniform Shell (m, n = 1, 2) Mode
(L_w data are derived from Equation 2, and plotted in Fig. 24.)

Frequency Hz	L_p dB	D dB/Sec	L_w dB
1033.6	64.3	7.29	62.9
1034.1	64.4		63.0
1034.7	64.7		63.3
1035.2	64.0		62.6
1035.7	63.6		62.2
1036.3	64.1		62.7
1036.8	63.8		62.4
1037.3	63.7	7.26	62.3
1037.5	63.9		62.5
1037.7	66.3		64.9
1038.3	63.9		62.6
1039.0	63.3	7.36	62.0
1039.4	63.6		62.3
1040.0	63.2		61.9
1040.5	63.7		62.4
1041.1	63.4		62.1
1041.7	63.4		62.1
1042.2	63.4		62.1
1042.8	64.4		63.1
1042.3	63.6	7.35	62.3

C. 4 Vibration Amplitude Versus Fringe Count

For time-average interferograms of subjects in sinusoidal motion taken with a helium-neon laser at wavelength 632. 8 nm, this gives the single-peak projected amplitude exactly for $\alpha = 0$ degrees and within 2 percent for $\alpha < 11$ degrees. For true amplitude, divide the table entry by the product $\cos \alpha \cdot \cos \theta$.

PROJECTED VIBRATION AMPLITUDE				
DARK FRINGE NUMBER	Inches x 10^{-6}		meters x 10^{-6}	Phase Excursion radians
	approx.	exact		
1	5	4. 768	. 1211	2. 405
2	11	10. 944	. 2780	5. 520
3	17	17. 156	. 4358	8.654
4	23	23. 377	. 5938	11. 792
5	30	29. 601	. 7519	14. 931
6	36	35. 827	. 9100	18. 071
7	42	42. 053	1. 0681	21. 212
8	48	48. 280	1. 2263	24. 352
9	55	54. 507	1. 3845	27. 493
10	61	60. 734	1. 5427	30. 635

REFERENCES

1. R. L. Powell and K. A. Stetson, J. Opt. Soc. Am., Vol. 55, 1965, pp. 1593-98, 1694-5.

2. N. E. Barnett, "Vibration Analysis by Hologram Interferometry," Engineering Acoustics Seminar, The Pennsylvania State University, University Park, Pennsylvania held January 19, 1967.

3. R. M. Grant, R. L. Lillie and N. E. Barnett, "Underwater Holography," J. Opt. Soc. Am., Vol. 56, 1966, p. 1142.

4. L. W. Orr, S. W. Tehon, and N. E. Barnett, "Isophase Surfaces in Interference Holography," Applied Optics, Vol. 7, 1968, pp. 202-3.

5. N. E. Barnett, "Progress Report on Vibration Analysis by Holographic Interferometry," paper WA 17 presented October 11, 1967, J. Opt. Soc. Am., Vol. 57, 1967, p. 1406A; also issued as report from Cooley Electronics Laboratory, Department of Electrical Engineering, The University of Michigan, Ann Arbor, January 1968.

6. N. E. Barnett, "Applications of Holographic Interferometry to Vibrating Cylindrical Shells," an invited paper presented at a two-day conference; "Holographic Interferometry: Its Application to Sonar Transducers," 1-2 August 1968, U. S. Navy Underwater Sound Laboratory, New London, Connecticut.

7. R. N. Arnold and G. B. Warburton, "Flexural Vibrations of the Walls of Thin Cylindrical Shells Having Freely Supported Ends," Proc. Roy. Soc. A., Vol. 197, 1949, p. 238.

8. N. E. Barnett, "The Efficacy of Damping Submerged Cylindrical Shells," Institute of Science and Technology report 3595-1-F, The University of Michigan, Ann Arbor, May 1962.